Higher-order finite element modeling of biological tissues under large strain conditions

Journal of Sound and Vibration 633 (2026) 119737

Contents lists available at ScienceDirect

Journal of Sound and Vibration

journal homepage: www.elsevier.com/locate/jsvi

Higher-order finite element modeling of biological tissues under large strain conditions

Piero Chiaia [1], Alfonso Pagani [2,*], Erasmo Carrera [3]

MUL² Lab, Department of Mechanical and Aerospace Engineering, Politecnico di Torino, Corso Duca degli Abruzzi, 10129, Torino, Italy

ARTICLE INFO

Keywords:
Carrera unified formulation
Beam elements
Plate elements
Biological tissue
Anisotropy
Linearized vibration

ABSTRACT

In this work, a unified numerical framework for the large strain and vibration analysis of biological tissues using high-order finite element (FE) models is presented. In this investigation, biological-like structural modeling is performed using refined FE based on the Carrera Unified Formulation (CUF) including anisotropy effects. The vibration behavior of soft tissues is analyzed including material anisotropy and large strains, examining the influence of pre-stress conditions on the modal response of such materials and structures. The governing equations in matrix form are derived using the Principle of Virtual Displacements (PVD) under a total Lagrangian formulation and solved via a Newton-Raphson linearization scheme. The energetic terms are rewritten in terms of Fundamental Nuclei (FN), which are independent of the theory of structural approximation, discretization models, and anisotropic hyperelastic constitutive potentials. Through several numerical examples, including the large strain and linearized vibration analyses of multilayered aortic materials, the accuracy and efficiency of the model are assessed by comparing the results against 3D elasticity solutions. The results highlight the potential and robustness of the CUF approach for examining equilibrium paths and the strongly nonlinear phenomena of cross-section deformation and modal interaction at large strains due to pre-stress effects, such as crossing and veering.

1. Introduction

Biological soft tissues such as arteries [1,2], ligaments and tendons [3,4], and prosthetic devices [5,6] play critical structural and functional roles in the human body. Their mechanical behavior is highly nonlinear, anisotropic, nearly incompressible, and strongly dependent on their microstructural organization [7]. The mechanical characterization of these materials and structures is fundamental for a wide range of biomedical engineering applications, including the design of prosthetic devices, surgical planning, injury prediction, and the development of computational tools for personalized medicine [8]. Accurate and valuable tools for the mechanical characterization of such materials not only enhance understanding but also enable the integration of biomechanics into diagnostics and device design.

Constitutive modeling of fiber-reinforced biological tissues has evolved significantly to capture the key features of their response under physiological loading conditions [9]. A major challenge is represented by the incorporation, within the

* Corresponding author.
E-mail addresses: piero.chiaia@polito.it (P. Chiaia), alfonso.pagani@polito.it (A. Pagani), erasmo.carrera@polito.it (E. Carrera).
[1] PhD student.
[2] Full Professor.
[3] Professor of Aerospace Structures and Aeroelasticity.

https://doi.org/10.1016/j.jsv.2026.119737
Received 10 September 2025; Received in revised form 3 January 2026; Accepted 25 February 2026
Available online 2 March 2026

constitutive model, of fiber dispersion effects, namely the statistical distribution of fiber orientations rather than the assumption of perfectly aligned fiber families [10], as proposed by the Holzapfel-Gasser-Ogden (HGO) model for anisotropic hardening [11]. These models have consistently been useful in replicating experimental results across various tissue types. Nevertheless, incorporating complex material behaviors, such as viscoelasticity [12], residual stresses [13], and remodeling [14], remains an active area of research.

In particular, in the context of functional soft materials and biological tissue modeling, many investigations have also included multi-physics interactions or the analysis of instability phenomena under external loading. Within this framework, particular interest has been directed toward the multi-physics simulation of biological tissues stimulated by thermal or electrical fields [15,16], where strong coupling effects provide overall tunable mechanical responses, particularly when exploiting the dielectric elastomers in tunable resonators, waveguides, or acoustic and vibration control [17–19]. Due to the complex constitutive behavior of such materials and structures, the multiphysics coupling in biological tissue analysis remains an active area of research to this day.

When dealing with functional biological tissues, one of the most discussed features is the asymmetric response of the collagen fibers when loaded in tension and compression, namely, collagen fibers are unable to carry any compression load. In this sense, a comprehensive review about the advances in constitutive modeling of such fibrous structures has been proposed by Holzapfel et al. [20]. Federico and Gasser [21] proposed the concept of mean average direction for dispersed fiber, including a Heaviside-like switch function to activate and exclude the compressed fibers. Melnik et al. [22] adopted the Generalized Structural Tensor (GST) approach for the compressed fiber exclusion, applying the statistical approach to axisymmetric dispersed fibers. Li et al. [23] analyzed the Angular Integration (AI) instead approach for excluding fibers under compression. However, it has been shown that the AI approach leads to computationally burdensome models that are not applicable even in realistic settings [23–25], thus the GST approach emerges as a more valuable and practical alternative. More recently, Li et al. [26] proposed a novel computational approach, based on the AI excluding method, to develop a numerical approach implemented in the FEAP finite element code to achieve accurate 3D fiber dispersion models. In available commercial softwares, other simplified procedures have been proposed to exclude compressed fibers, as implemented in the built-in HGO model in ABAQUS. However, the switch function adopted in the ABAQUS model, based on the use of Macauley parentheses, leads to inappropriate results since it is based on the use of the rescaled stretch in the fiber direction and does not penalize the specific stretch contribution of the generalized structural tensor [27]. Similar considerations have been addressed by Vergori et al. [28], where the authors showed that the built-in HGO model does not predict the real physical response of anisotropic hyperelastic spheres in the small strain regime when subjected to hydrostatic pressure. An energetic approach for the analysis of anisotropic hyperelastic media has also been developed by Federico et al. [29].

The nonlinear nature of the governing equations, combined with the anisotropic and heterogeneous structure of tissues, makes analytical approaches not suitable for real-world applications. Due to the complexity of developed constitutive models, analytical solutions are available only for simple, idealized problems [30,31], thus numerical models have become necessary for analyzing biological structures. Recent advances in the FE modeling of such materials have been proposed in many works, see [32–36]. Finite element simulations of biological tissues commonly use classical 3D FE models, but their limitations, such as aspect-ratio constraints and susceptibility to volumetric locking, lead to the adoption of fine meshes and high computational cost despite offering direct solutions of the equilibrium equations without any superimposed kinematic assumptions [37].

The present work aims to analyze the vibration properties of soft biological tissues, leveraging on the capabilities of the already established refined nonlinear higher-order beam (1D) and plate (2D) models, implemented in the Carrera Unified Formulation (CUF) [38], including nonlinear constitutive laws and anisotropic effects (such as collagen fiber stiffening at large strain), to characterize the modal behavior of biological-like structures fully. Based on a recursive index notation, the formalism introduced by CUF allows for rewriting the governing equations in terms of Fundamental Nuclei (FN), the elementary blocks of the present approach, independent of discretization model employed and the displacement field assumptions considered [39,40]. The proposed approach has also been recently extended to the material nonlinear analysis of hyperelastic isotropic and fiber-reinforced structures, through the adoption of both 1D and 2D beam and plate models in the case of static and linearized vibration analysis of pre-stressed isotropic hyperelastic media [41,42].

When dealing with pre-stressed structures, in a fully nonlinear context, instability-induced phenomena are encountered, such as snap-through or wrinkling [43]. Over the years, many numerical and experimental dynamical approaches for the analysis of the critical behavior of structures near instability points have been proposed, such as the Vibration Correlation Technique (VCT) [44], which exploits the modal properties of pre-stressed structures to analyze bifurcation and critical points. Leveraging the capabilities of the structural modeling approach enabled by CUF, this approach has also been successfully applied within the framework of higher-order CUF models, as in [45,46]. In this work, the established framework is now extended to the static and modal analysis in non-trivial equilibrium states of biological tissues, discussing the implementation of any hyperelastic models in a general FE framework and the influence of anisotropy, geometry, and boundary conditions for the modal behavior of such materials and structures. In this sense, an efficient and accurate numerical tool for the analysis of pre-stressed biological-like structures is here proposed.

The work is organized as follows: (i) the mathematical preliminaries and hyperelastic approach based on classical continuum mechanics arguments are presented in Section 2; (ii) the Unified formulation of beam and plate theories is described in Section 3; (iii) the proposed FE model based and the derivation procedure, through the Principle of Virtual Displacements (PVD), of the weak-form governing equations for the static and modal problems is presented in Section 4; (iv) three numerical test cases dealing with fiber-reinforced beam and plate structures are presented and discussed in Section 5; (v) finally, the conclusions are drawn in Section 6.

2. Preliminaries

2.1. Kinematics

Let Ω_0 be the closed volume of the reference configuration of a continuum body. Denote with $\boldsymbol{X}$ the position vector of the material particles within Ω_0 with respect to the material Cartesian reference frame. After deformation, the continuum body identifies the region Ω as the actual configuration, whose material particles are now denoted by $\boldsymbol{x}$. Let also $\chi : \boldsymbol{X} \in \Omega_0 \rightarrow \boldsymbol{x} \in \Omega$ be the definition of deformation, mapping the material points of reference and actual configurations. Denote now the deformation gradient with $\mathbf{F} = \partial\chi/\partial\boldsymbol{X}$ and the volume ratio $J = \det \mathbf{F}$.

According to the Flory decomposition introduced in Flory [47], the deformation gradient can be uniquely decomposed into its volumetric and distortional (isochoric) part, as well as the right Cauchy-Green strain tensor $\mathbf{C} = \mathbf{F}^T\mathbf{F}$:

$$\mathbf{F} = \mathbf{F}_{vol}\bar{\mathbf{F}} = (J^{1/3}\mathbf{I})\bar{\mathbf{F}}, \quad \bar{\mathbf{F}} = J^{-1/3}\mathbf{F} \tag{1}$$

$$\mathbf{C} = \mathbf{C}_{vol}\bar{\mathbf{C}} = (J^{2/3}\mathbf{I})\bar{\mathbf{C}}, \quad \bar{\mathbf{C}} = J^{-2/3}\mathbf{C} \tag{2}$$

where $\bar{\mathbf{F}}$ and $\bar{\mathbf{C}}$ denote the rescaled deformation gradient and Cauchy-Green strain tensor, respectively, and $\mathbf{F}_{vol}$ and $\mathbf{C}_{vol}$ are the volumetric components. Within the continuum mechanics framework, including an anisotropic, nonlinear constitutive law, the effects of fiber reinforcement must be accounted for. It is assumed that continuous distributions of fibers aligned along reference unit vectors are embedded within the continuum body [1]. For a material with two families of embedded fibers, the unit vectors $\boldsymbol{a}_0$ and $\boldsymbol{g}_0$ denote the directions along which the two fibers are defined in the material reference configuration. The fiber directions in the actual reference frame are retrieved by means of the deformation χ, introducing the direction $\boldsymbol{a} = \mathbf{F}\boldsymbol{a}_0$ and $\boldsymbol{g} = \mathbf{F}\boldsymbol{g}_0$, alongside the stretch of the fibers [11]. For further considerations, here the isotropic and fiber-related invariants of the deformation are introduced, starting from the right Cauchy-Green strain tensor:

$$I_1 = \mathrm{tr}(\mathbf{C}), \quad I_2 = \frac{1}{2}((\mathrm{tr}(\mathbf{C}))^2 - \mathrm{tr}(\mathbf{C}^2)), \quad I_3 = \det(\mathbf{C}) = \det(\mathbf{F}^T\mathbf{F}) = J^2 \tag{3}$$

$$I_4 = \boldsymbol{a}_0 \cdot \mathbf{C}\boldsymbol{a}_0, \quad I_5 = \boldsymbol{a}_0 \cdot \mathbf{C}^2\boldsymbol{a}_0 \tag{4}$$

$$I_6 = \boldsymbol{g}_0 \cdot \mathbf{C}\boldsymbol{g}_0, \quad I_7 = \boldsymbol{g}_0 \cdot \mathbf{C}^2\boldsymbol{g}_0 \tag{5}$$

Here, $\det(\cdot)$ and $\mathrm{tr}(\cdot)$ denote the determinant and trace operators, respectively. The invariants I_4 and I_6 are related to the pure stretch measures for the two fiber families, specifically $\lambda_{\boldsymbol{a}_0}$ and $\lambda_{\boldsymbol{g}_0}$, where λ denotes fiber stretch along $\boldsymbol{a}_0$ or $\boldsymbol{g}_0$. These invariant quantities are similarly defined using the rescaled Cauchy-Green strain tensor, $\bar{I}_j = J^{-2/3}I_j$ for $j = 1, 4, 6$ and $\bar{I}_k = J^{-4/3}I_k$ for $k = 2, 5, 7$.

2.2. Anisotropic hyperelastic constitutive law

The mechanical behavior of biological soft tissue is modeled within the framework of anisotropic hyperelasticity, introducing the Helmholtz free energy Ψ (strain energy density) defined per unit reference volume. In general, it depends on the invariants and pseudo-invariants of the deformation. The continuous fiber reinforcement effects are accounted for in the strain energy potential by introducing the general second-order structural tensors, depending on the fiber directions:

$$\Psi = \Psi(\mathbf{C}, \boldsymbol{a}_0 \otimes \boldsymbol{a}_0, \boldsymbol{g}_0 \otimes \boldsymbol{g}_0) = \Psi_{vol}(J) + \bar{\Psi}(\bar{\mathbf{C}}, \boldsymbol{a}_0 \otimes \boldsymbol{a}_0, \boldsymbol{g}_0 \otimes \boldsymbol{g}_0) \tag{6}$$

where $(\cdot) \otimes (\cdot)$ stands for the dyadic product operator and the decoupled expression of strain energy functions [47] is considered again; namely, Ψ is written as the sum of purely independent components representing each different material behavior:

$$\Psi = \Psi_{vol}(J) + \bar{\Psi}_{iso}(\bar{I}_1, \bar{I}_2) + \bar{\Psi}_{aniso}(\bar{I}_1, \bar{I}_2, \bar{I}_4, \bar{I}_5, \bar{I}_6, \bar{I}_7) \tag{7}$$

The reader is referred to Holzapfel [48] for a detailed description of the approach. Considering the material model given by the expression of the strain energy function, the constitutive law in the material reference frame is obtained following the Coleman-Noll procedure, obtaining the standard relation for the second Piola-Kirchhoff (PK2) stress tensor $\mathbf{S} = 2\partial\Psi/\partial\mathbf{C}$, written again following the decoupled approach:

$$\mathbf{S} = 2\frac{\partial\Psi}{\partial\mathbf{C}} = 2\frac{\partial\Psi_{vol}}{\partial\mathbf{C}} + 2\frac{\partial\bar{\Psi}}{\partial\mathbf{C}} = \mathbf{S}_{vol} + \mathbf{S}_{iso} \tag{8}$$

where the two terms of the PK2 stress tensor are respectively defined as:

$$\mathbf{S}_{vol} = 2\frac{\partial\Psi_v(J)}{\partial\mathbf{C}} = Jp\mathbf{C}^{-1} \tag{9}$$

$$\mathbf{S}_{iso} = 2\frac{\partial\bar{\Psi}}{\partial\mathbf{C}} = 2\frac{\partial\bar{\Psi}}{\partial\bar{\mathbf{C}}} \cdot \frac{\partial\bar{\mathbf{C}}}{\partial\mathbf{C}} = J^{-2/3}\left(\mathbb{I} - \frac{1}{3}\mathbf{C}^{-1} \otimes \mathbf{C}\right) : \bar{\mathbf{S}} = J^{-2/3}\mathbb{P} : \bar{\mathbf{S}} \tag{10}$$

where $\bar{\mathbf{S}}$ is the rescaled second Piola-Kirchoff stress tensor (RPK2), $\mathbb{P}$ is the projection tensor used in the Total Lagrangian approach for hyperelasticity (dependence from the reference configuration), p is the hydrostatic pressure and ":" denotes the double contraction operator between tensors. The mechanical characterization of the constitutive law is given by the explicit expression of the RPK2 tensor, whose explicit expression is given from the derivatives of the strain energy function with respect to the rescaled invariants:

$$\bar{\mathbf{S}} = 2\left[\left(\frac{\partial\bar{\Psi}}{\partial\bar{I}_1} + \bar{I}_1\frac{\partial\bar{\Psi}}{\partial\bar{I}_2}\right)\mathbf{I} - \frac{\partial\bar{\Psi}}{\partial\bar{I}_2}\mathbf{C} + \frac{\partial\bar{\Psi}}{\partial\bar{I}_4}\boldsymbol{a}_0\otimes\boldsymbol{a}_0 + \frac{\partial\bar{\Psi}}{\partial\bar{I}_5}\left(\boldsymbol{a}_0\otimes\bar{\mathbf{C}}\boldsymbol{a}_0 + \boldsymbol{a}_0\bar{\mathbf{C}}\otimes\boldsymbol{a}_0\right) + \frac{\partial\bar{\Psi}}{\partial\bar{I}_6}\boldsymbol{g}_0\otimes\boldsymbol{g}_0 + \frac{\partial\bar{\Psi}}{\partial\bar{I}_7}\left(\boldsymbol{g}_0\otimes\bar{\mathbf{C}}\boldsymbol{g}_0 + \boldsymbol{g}_0\bar{\mathbf{C}}\otimes\boldsymbol{g}_0\right)\right] \tag{11}$$

Generally, in the development of a finite element formulation for (nonlinear) material constitutive laws such as hyperelasticity and large strain problems, the tangent elasticity tensor has to be derived under a consistent linearization of the constitutive law. To solve the nonlinear governing equations using iterative-incremental numerical approaches, the tangent elasticity tensor is introduced to account for both geometric and material nonlinearities. The constitutive law Eq. (8) is written in incremental form introducing the tangent elasticity tensor $\mathbb{C}$:

$$\Delta\mathbf{S} = \mathbb{C} : \frac{1}{2}\Delta\mathbf{C}, \quad \mathbb{C} = 2\frac{\partial\mathbf{S}(\mathbf{C})}{\partial\mathbf{C}} \tag{12}$$

Assuming the volumetric-deviatoric splitting for the tensor $\mathbb{C}$ again, the two terms are separately treated and defined following the classical derivation procedure, as presented for the PK2 stress tensor:

$$\mathbb{C} = 2\frac{\partial\mathbf{S}}{\partial\mathbf{C}} = 2\frac{\partial\mathbf{S}_v}{\partial\mathbf{C}} + 2\frac{\partial\mathbf{S}_{iso}}{\partial\mathbf{C}} = \mathbb{C}_{vol} + \mathbb{C}_{iso} \tag{13}$$

The closed-form expression depending on the physical quantities previously introduced is carried out and expressed as done in [48]:

$$\mathbb{C}_{vol} = J\left(p + J\frac{dp}{dJ}\right)\mathbf{C}^{-1}\otimes\mathbf{C}^{-1} - 2Jp\mathbf{C}^{-1}\odot\mathbf{C}^{-1} \tag{14}$$

$$\mathbb{C}_{iso} = \mathbb{P} : \bar{\mathbb{C}} : \mathbb{P}^T + \frac{2}{3}J^{-2/3}(\bar{\mathbf{S}} : \mathbf{C})\tilde{\mathbb{P}} - \frac{2}{3}(\mathbf{C}^{-1}\otimes\mathbf{S}_{iso} + \mathbf{S}_{iso}\otimes\mathbf{C}^{-1}) \tag{15}$$

where the symbol $(\cdot)\odot(\cdot)$ stands for the Hadamard product, $\bar{\mathbb{C}}$ is the fictitious rescaled tangent elasticity tensor, defined as done for the RPK2 tensor function of the invariants of the deformation, and $\tilde{\mathbb{P}}$ is the modified projection tensor defined as:

$$\tilde{\mathbb{P}} = \mathbf{C}^{-1}\odot\mathbf{C}^{-1} - \frac{1}{3}\mathbf{C}^{-1}\otimes\mathbf{C}^{-1} \tag{16}$$

The reader is again referred to Holzapfel [48] for more details on the derivation of the tangent elasticity tensor.

These introduced physical quantities are the starting point for the implementation of a fully nonlinear finite element scenario for biological tissue modeling, where the constitutive law and its linearization are expressed in terms of invariants of the deformation to implement any hyperelastic strain energy function model straightforwardly.

3. Unified formulation of beam and plate theories

Refined higher-order beam (1D) and plate (2D) CUF models are here briefly introduced. The implementation of any theory-of-structure based FE models is presented in the well-established CUF framework [39].

The key feature of the CUF formalism is the recursive index notation for the polynomial expansion of the three-dimensional displacement field. Within this context, the introduction of generalized nodal displacements enables straightforward implementation of any structural approximation theory along the beam cross-section or plate thickness, without the need for ad hoc mathematical formalism to define strain, stress, and stiffness components. This recursive expansion technique allows the implementation of any higher-order theory of structure. The Cartesian three-dimensional displacement field for a beam and plate model is exploited as:

$$\text{Beam 1D models: } \boldsymbol{u}(x,y,z) = F_\tau(x,z)\boldsymbol{u}_\tau(y) \quad \tau = 1,\dots,M \tag{17}$$

$$\text{Plate 2D models: } \boldsymbol{u}(x,y,z) = F_\tau(z)\boldsymbol{u}_\tau(x,y) \quad \tau = 1,\dots,M \tag{18}$$

where M denotes the dimension of the polynomial expansion basis, which is associated with the polynomial order of approximation of the structural theory, F_τ is the set of expansion functions, and $\boldsymbol{u}_\tau$ is the vector of generalized displacement components along the expansion directions.

In the present work, the beam cross-section and plate thickness kinematics are described by means of Lagrange's expansion polynomials (LE-models). Within this context, pure displacement-based models for cross-sectional or thickness expansions are developed using an isoparametric approach. In the following, linear, parabolic, and cubic expansion models will be adopted. In the case of 1D-CUF LE expansion models, the set of interpolating functions across the beam cross-section will be denoted as four-node linear (L4), nine-node parabolic (L9), and six-node quadratic (L16). In 2D-CUF LE expansion models, the one-dimensional interpolations along the plate thickness are linear (LE1), parabolic (LE2), and cubic (LE3), respectively. In the present approach, the generalized displacements of the CUF expansion $\boldsymbol{u}_\tau = (u_{x_\tau}, u_{y_\tau}, u_{z_\tau})$ are represented by the Cartesian displacement components of the Lagrange Point defined along the beam cross-section or plate thickness local subdomain. A graphical representation of the proposed LE-class 1D and 2D CUF models is provided in Fig. 1.

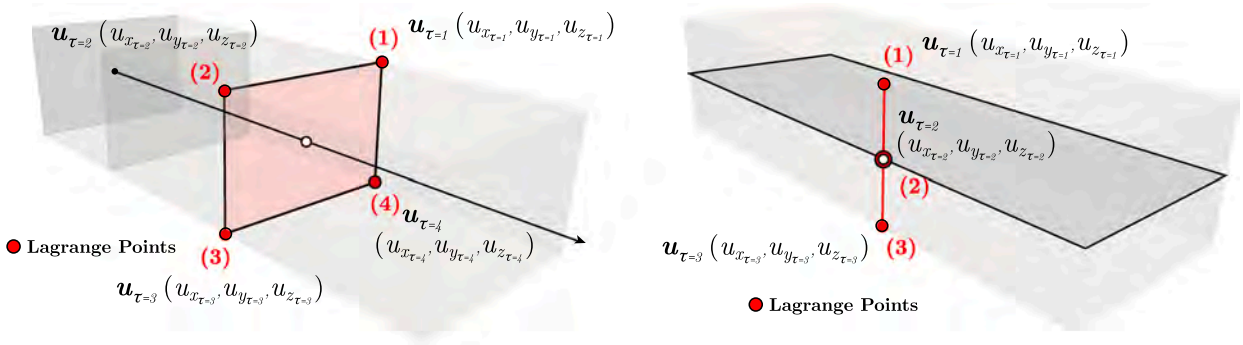

(a) 1D LE-class models **(b)** 2D LE-class models

Fig. 1. CUF LE-class models, graphical representation of the mathematical model.

Here, as an example, the parabolic interpolation with a single L9 subdomain along the beam cross-section is provided:

$$\text{1D:}\begin{cases} u_x(x,y,z) = F_1(x,z)u_{x_{\tau=1}}(y) + F_2(x,z)u_{x_{\tau=2}}(y) + \cdots + F_9(x,z)u_{x_{\tau=9}}(y) \\ u_y(x,y,z) = F_1(x,z)u_{y_{\tau=1}}(y) + F_2(x,z)u_{y_{\tau=2}}(y) + \cdots + F_9(x,z)u_{y_{\tau=9}}(y) \\ u_z(x,y,z) = F_1(x,z)u_{z_{\tau=1}}(y) + F_2(x,z)u_{z_{\tau=2}}(y) + \cdots + F_9(x,z)u_{z_{\tau=9}}(y) \end{cases} \tag{19}$$

where the set of 2D parabolic Lagrange polynomials, defined in the natural coordinate system (ξ, η), mapping to the domain (x, z), is:

$$F_\tau(\xi,\eta) = \frac{1}{4}(\xi^2 + \xi\xi_i)(\eta^2 + \eta\eta_i), \quad \tau = 1,3,5,7 \tag{20}$$

$$F_\tau(\xi,\eta) = \frac{1}{2}\xi_i^2(\xi^2 + \xi\xi_i)(1-\eta^2) + \frac{1}{2}\eta_i^2(\eta^2 + \eta\eta_i)(1-\xi^2), \quad \tau = 2,4,6,8 \tag{21}$$

$$F_\tau(\xi,\eta) = (1-\xi^2)(1-\eta^2), \quad \tau = 9 \tag{22}$$

Instead, the parabolic interpolation with a single LE2 subdomain along the plate thickness will be written as:

$$\text{2D:}\begin{cases} u_x(x,y,z) = F_1(z)u_{x_{\tau=1}}(x,y) + F_2(z)u_{x_{\tau=2}}(x,y) + F_3(z)u_{x_{\tau=3}}(x,y) \\ u_y(x,y,z) = F_1(z)u_{y_{\tau=1}}(x,y) + F_2(z)u_{y_{\tau=2}}(x,y) + F_3(z)u_{y_{\tau=3}}(x,y) \\ u_z(x,y,z) = F_1(z)u_{z_{\tau=1}}(x,y) + F_2(z)u_{z_{\tau=2}}(x,y) + F_3(z)u_{z_{\tau=3}}(x,y) \end{cases} \tag{23}$$

where the set of parabolic 1D Lagrange polynomials, defined in the natural domain by means of the variable ν, is:

$$N_1(\nu) = \frac{1}{2}(\nu^2 - \nu); \quad N_2(\nu) = -\nu^2 + 1; \quad N_3(\nu) = \frac{1}{2}(\nu^2 + \nu); \tag{24}$$

The adoption of LE models has been referred to as the Component-Wise (CW) or Layer-Wise (LW) modeling of structures [39]. By adopting such models, different cross-section sub-components or plate layers are modeled independently, defining independent displacement fields and imposing displacement continuity at the nodal level where superposition is required. The reader is addressed to Carrera et al. [39] for a more detailed description of LE-class models.

Alongside the introduction of a refined theory of structure approximation, the generalized displacement field components of the 1D and 2D CUF beam and plate models are further discretized by the classical FE approaches:

$$\text{Beam 1D models:} \quad \boldsymbol{u}_\tau(y) = N_i(y)\boldsymbol{u}_{\tau i} \quad i = 1,\ldots,N_n \tag{25}$$

$$\text{Plate 2D models:} \quad \boldsymbol{u}_\tau(x,y) = N_i(x,y)\boldsymbol{u}_{\tau i} \quad i = 1,\ldots,N_n \tag{26}$$

where the N_i shape functions defined over the N_n number of finite nodes are adopted for the interpolation of the generalized displacement along the beam axis or plate reference mid-surface. In the case of LE models, the final discrete unknowns of the problems $\boldsymbol{u}_{\tau i}$ represent the pure Cartesian nodal displacements. In Eq. (26), the index i is adopted for the summation along the finite nodes per element of 1D beam axis or 2D plate mid-surface discretization.

The final 3D displacement field in the CUF framework is then expressed as a coupled expansion of refined structural theories and FE approximation along the reference directions:

$$\text{Beam 1D models:} \quad \boldsymbol{u}(x,y,z) = F_\tau(x,z)\boldsymbol{u}_\tau(y) = F_\tau(x,z)N_i(y)\boldsymbol{u}_{\tau i} \tag{27}$$

$$\text{Plate 2D models:} \quad \boldsymbol{u}(x,y,z) = F_\tau(z)\boldsymbol{u}_\tau(x,y) = F_\tau(z)N_i(x,y)\boldsymbol{u}_{\tau i} \tag{28}$$

In our proposed model, the FE approximation of the beam axis will be addressed as linear B2, parabolic B3, and cubic B4 finite elements; instead, the approximation along the plate mid-surface will be referred to as linear Q4, parabolic Q9, and cubic Q16, indicating the total number of finite nodes adopted in the single element definition. Eq. (28) is the most general expression of the displacement field that defines high-order and refined finite element models for beam and plate structures in a hierarchical manner,

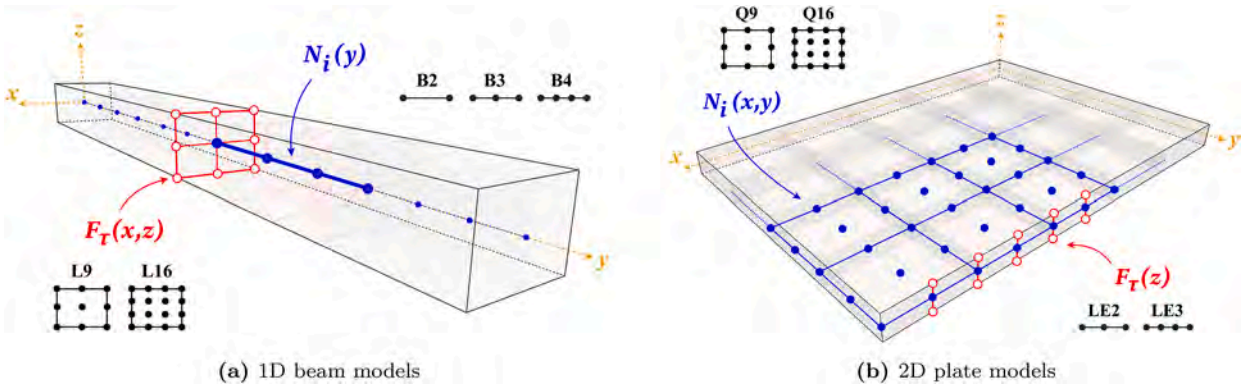

Fig. 2. High order 1D and 2D CUF models.

since it is independent of the polynomial basis adopted in the kinematics of the beam axis or plate mid-surface and expansion theories considered. A graphical representation of higher-order 1D and 2D CUF models, where both the theory of structure approximation and FE modeling are considered, is provided in Fig. 2.

4. Governing equations for the static and vibration problem

4.1. Unified matrix form of physical quantities

In the present work, a Total Lagrangian FE procedure for anisotropic hyperelastic structures is considered. For this reason, the balance equation in weak form is defined in terms of the work-conjugate of the Cauchy-Green strain tensor, the kinematic measure adopted in the material reference frame, namely the PK2 stress tensor. Voigt's notation for symmetric tensors is now considered in the definition of physical quantities:

$$\mathbf{S} = \{S_{xx}, S_{yy}, S_{zz}, S_{xz}, S_{yz}, S_{xy}\}^T \tag{29}$$

$$\mathbf{E} = \{E_{xx}, E_{yy}, E_{zz}, E_{xz}, E_{yz}, E_{xy}\}^T \tag{30}$$

The components of the Green-Lagrange strain tensor are naturally derived from the generalized nodal displacements and rewritten in terms of recursive CUF expansion. Suppressing the variable dependence to obtain a more general formulation of the strain tensor, independent of the 1D or 2D model choice, one can rewrite:

$$\mathbf{E} = (\mathbf{b}_l + \mathbf{b}_{nl})\boldsymbol{u} = (\mathbf{b}_l + \mathbf{b}_{nl})F_\tau N_i \boldsymbol{u}_{\tau i} = \left(\mathbf{B}_l^{\tau i} + \mathbf{B}_{nl}^{\tau i}\right)\boldsymbol{u}_{\tau i} \tag{31}$$

The formal matrices of derivatives operator $\mathbf{b}_l$ and $\mathbf{b}_{nl}$, whose expression can be found in Pagani and Carrera [49], are the mathematical operators that provide the algebraic matrices $\mathbf{B}_l^{\tau i}$ and $\mathbf{B}_{nl}^{\tau i}$, from which the strain components are retrieved starting from the polynomial expansion of the displacement field. These matrices are here specialized for both beam and plate models, imposing the variable dependence of the two polynomial bases:

1D CUF beam models

$$\mathbf{B}_l^{\tau i} = \begin{bmatrix} F_{\tau,x}N_i & 0 & 0 \\ 0 & F_\tau N_{i,y} & 0 \\ 0 & 0 & F_{\tau,z}N_i \\ F_{\tau,z}N_i & 0 & F_{\tau,x}N_i \\ 0 & F_{\tau,z}N_i & F_\tau N_{i,y} \\ F_\tau N_{i,y} & F_{\tau,x}N_i & 0 \end{bmatrix} \tag{32}$$

$$\mathbf{B}_{nl}^{\tau i} = \frac{1}{2}\begin{bmatrix} u_{x,x}F_{\tau,x}N_i & u_{y,x}F_{\tau,x}N_i & u_{z,x}F_{\tau,x}N_i \\ u_{x,y}F_\tau N_{i,y} & u_{y,y}F_\tau N_{i,y} & u_{z,y}F_\tau N_{i,y} \\ u_{x,z}F_{\tau,z}N_i & u_{y,z}F_{\tau,z}N_i & u_{z,z}F_{\tau,z}N_i \\ u_{x,x}F_{\tau,z}N_i + u_{x,z}F_{\tau,x}N_i & u_{y,x}F_{\tau,z}N_i + u_{y,z}F_{\tau,x}N_i & u_{z,x}F_{\tau,z}N_i + u_{z,z}F_{\tau,x}N_i \\ u_{x,y}F_{\tau,z}N_i + u_{x,z}F_\tau N_{i,y} & u_{y,y}F_{\tau,z}N_i + u_{y,z}F_\tau N_{i,y} & u_{z,y}F_{\tau,z}N_i + u_{z,z}F_\tau N_{i,y} \\ u_{x,x}F_\tau N_{i,y} + u_{x,y}F_{\tau,x}N_i & u_{y,x}F_\tau N_{i,y} + u_{y,y}F_{\tau,x}N_i & u_{z,x}F_\tau N_{i,y} + u_{z,y}F_{\tau,x}N_i \end{bmatrix} \tag{33}$$

2D CUF plate models

$$\mathbf{B}_l^{\tau i} = \begin{bmatrix} F_\tau N_{i,x} & 0 & 0 \\ 0 & F_\tau N_{i,y} & 0 \\ 0 & 0 & F_{\tau,z} N_i \\ F_{\tau,z} N_i & 0 & F_\tau N_{i,x} \\ 0 & F_{\tau,z} N_i & F_\tau N_{i,y} \\ F_\tau N_{i,y} & F_\tau N_{i,x} & 0 \end{bmatrix} \tag{34}$$

$$\mathbf{B}_{nl}^{\tau i} = \frac{1}{2} \begin{bmatrix} u_{x,x} F_\tau N_{i,x} & u_{y,x} F_\tau N_{i,x} & u_{z,x} F_\tau N_{i,x} \\ u_{x,y} F_\tau N_{i,y} & u_{y,y} F_\tau N_{i,y} & u_{z,y} F_\tau N_{i,y} \\ u_{x,z} F_{\tau,z} N_i & u_{y,z} F_{\tau,z} N_i & u_{z,z} F_{\tau,z} N_i \\ u_{x,x} F_{\tau,z} N_i + u_{x,z} F_\tau N_{i,x} & u_{y,x} F_{\tau,z} N_i + u_{y,z} F_\tau N_{i,x} & u_{z,x} F_{\tau,z} N_i + u_{z,z} F_\tau N_{i,x} \\ u_{x,y} F_{\tau,z} N_i + u_{x,z} F_\tau N_{i,y} & u_{y,y} F_{\tau,z} N_i + u_{y,z} F_\tau N_{i,y} & u_{z,y} F_{\tau,z} N_i + u_{z,z} F_\tau N_{i,y} \\ u_{x,x} F_\tau N_{i,y} + u_{x,y} F_\tau N_{i,x} & u_{y,x} F_\tau N_{i,y} + u_{y,y} F_\tau N_{i,x} & u_{z,x} F_\tau N_{i,y} + u_{z,y} F_\tau N_{i,x} \end{bmatrix} \tag{35}$$

where the symbol $(\cdot)_{,(\cdot)}$ stands for the partial derivative operator.

To define the terms related to the energetic contributions in the variational principles, which will be introduced later, the virtual variation of the displacement field is now introduced. Exploiting the same index notation adopted for the displacement field, the virtual variations of displacement and strain components are explicitly derived, adopting the j index for kinematic models along the beam axis and plate mid-surface, and the s index for the CUF theory of structure approximation expansion:

$$\delta \boldsymbol{u}(x, y, z) = F_s \delta \boldsymbol{u}_s = F_s N_j \delta \boldsymbol{u}_{sj} \quad j = 1, 2, \ldots, N_n, \quad s = 1, \ldots, M \tag{36}$$

$$\delta \mathbf{E} = \delta \Big((\mathbf{B}_l^{\tau i} + \mathbf{B}_{nl}^{\tau i}) \boldsymbol{u}_{\tau i} \Big) = \Big(\mathbf{B}_l^{sj} + 2\mathbf{B}_{nl}^{sj} \Big) \delta \boldsymbol{u}_{sj} \tag{37}$$

Again, the algebraic matrices $\mathbf{B}_l^{sj}$ and $\mathbf{B}_{nl}^{sj}$ are defined as done in Eq. (31), applying the formal matrices of derivative operators to the polynomial expansion used for the virtual displacement field.

4.2. Principle of virtual displacements

In the present work, the derivation of the governing equation in weak form is carried out by means of PVD. Supposing negligible body volume forces, PVD states:

$$\delta \mathcal{L}_{int} + \delta \mathcal{L}_{ine} = \delta \mathcal{L}_{ext} \tag{38}$$

where δ denotes the virtual variation and $\mathcal{L}_{int}$, $\mathcal{L}_{ext}$, and $\mathcal{L}_{ine}$ denote the work of the internal, external, and inertia loads, respectively. These energetic contributions are defined in compact form as:

$$\text{(a)}\ \delta \mathcal{L}_{int} = \int_{\Omega_0} \delta \mathbf{E}^T \mathbf{S} dV \quad \text{(b)}\ \delta \mathcal{L}_{ext} = \int_{\Omega_0} \delta \boldsymbol{u}^T \boldsymbol{f} dV \quad \text{(c)}\ \delta \mathcal{L}_{ine} = \int_{\Omega_0} \delta \boldsymbol{u}^T \rho \ddot{\boldsymbol{u}} dV \tag{39}$$

where $\mathbf{S}$ is the PK2 stress tensor, $\mathbf{E}$ is the Green-Lagrange strain tensor, $\boldsymbol{f}$ is the vector of external loads, and $\ddot{\boldsymbol{u}}$ is the acceleration vector. In a Total Lagrangian FE approach, all volume integrals are computed with respect to the material (or reference) configuration.

Starting from these definitions, the basic building blocks of the present modeling approach can be introduced. Imposing now the discretization proposed for the physical quantities, introduced previously, the matrix form of these terms is rewritten by means of the Fundamental Nuclei (FN), elementary matrices that are defined independently of the mathematical model imposed within the FE definition.

The internal strain energy Eq. (39)(a) is rewritten as:

$$\delta \mathcal{L}_{int} = \int_{\Omega_0} \delta \boldsymbol{u}_{sj}^T \Big(\mathbf{B}_l^{sj} + 2\mathbf{B}_{nl}^{sj} \Big)^T \boldsymbol{S} dV = \delta \boldsymbol{u}_{sj}^T \left[\int_{\Omega_0} \Big(\mathbf{B}_l^{sj} + 2\mathbf{B}_{nl}^{sj} \Big)^T \mathbf{S} dV \right] = \delta \boldsymbol{u}_{sj}^T \mathbf{F}_{int}^{sj} \tag{40}$$

where $\mathbf{F}_{int}^{sj}$ the 3x1 FN of the internal forces vector:

$$\mathbf{F}_{int}^{sj} = \int_{\Omega_0} \Big(\mathbf{B}_l^{sj} + 2\mathbf{B}_{nl}^{sj} \Big)^T \mathbf{S} dV \tag{41}$$

The external load term Eq. (39)(b) is rewritten as:

$$\delta \mathcal{L}_{ext} = \int_{\Omega_0} \delta \boldsymbol{u}^T \boldsymbol{f} dV = \int_{\Omega_0} \delta \boldsymbol{u}_{sj}^T F_s N_j \boldsymbol{f} dV = \delta \boldsymbol{u}_{sj}^T \mathbf{F}_{ext}^{sj} \tag{42}$$

where $\mathbf{F}_{ext}^{sj}$ the 3x1 FN of the external forces vector:

$$\mathbf{F}_{ext}^{sj} = \int_{\Omega_0} F_s N_j \boldsymbol{f} dV \tag{43}$$

The linear interial term Eq. (39)(c) is:

$$\delta\mathcal{L}_{ine} = \int_{\Omega_0} \delta\boldsymbol{u}^T \rho\, \ddot{\boldsymbol{u}} dV = \int_{\Omega_0} \delta\boldsymbol{u}_{sj}^T F_s N_j \rho F_\tau N_i \ddot{\boldsymbol{u}}_{\tau i} dV = \delta\boldsymbol{u}_{sj}^T \mathbf{M}^{\tau sij} \ddot{\boldsymbol{u}}_{\tau i} \tag{44}$$

where $\mathbf{M}^{\tau sij}$ the 3x3 FN of the constant mass matrix:

$$\mathbf{M}^{\tau sij} = \int_{\Omega_0} F_s N_j\, \rho\, \mathbf{I}\, F_\tau N_i\, dV \tag{45}$$

Substituting then Eqs. (40), (42) and (45), the variational principle is written in matrix form:

$$\delta\boldsymbol{u}_{sj} : \quad \mathbf{F}_{int}^{sj} + \mathbf{M}^{\tau sij} \ddot{\boldsymbol{u}}_{\tau i} = \mathbf{F}_{ext}^{sj} \tag{46}$$

The key feature of the proposed approach, enabled by CUF, is the definition of FE matrices independently of the assumed displacement field. The definitions of the FN are introduced regardless of the kinematic models adopted along the beam axis or the plate mid-surface, as well as the theory of structural approximation along the beam cross-section or the plate thickness. These elementary matrices, defined for any arbitrary polynomial expansion, are then specialized and computed by assigning the specific set of polynomial expansion regarding the N_i, N_j, F_τ, and F_s polynomial basis. Exploiting the summation over the recursive indices expansion, thus looping on the four introduced indices, the classical FE matrices are retrieved and assembled by following classical stiffness matrices assembling arguments. More details about the generic expansion and assembling procedure of the FN can be found in [39]. Assembling the FE matrices along the discretization considered, the final definition of PVD in matrix form states:

$$\mathbf{F}_{int}(\boldsymbol{u}) + \mathbf{M}\ddot{\boldsymbol{u}} = \mathbf{F}_{ext}(\boldsymbol{f}) \tag{47}$$

4.3. Linearized-incremental governing equations

In any FE scenario for hyperelastic materials, because the constitutive relations involve both geometric and material nonlinearities, the nonlinear equilibrium equations are strongly nonlinear. Hence, the final governing equations are typically solved using numerical incremental-iterative methods based on linearization. Starting from Eq. (47), the unbalanced nodal force vector is defined as:

$$\boldsymbol{\varphi}_{res}(\boldsymbol{u}, \ddot{\boldsymbol{u}}, \boldsymbol{f}) = \mathbf{F}_{int} + \mathbf{M}\ddot{\boldsymbol{u}} - \mathbf{F}_{ext} \tag{48}$$

With this formalism, an equilibrium state is expressed by the condition $\boldsymbol{\varphi}_{res}(\boldsymbol{u}, \ddot{\boldsymbol{u}}, \boldsymbol{f}) = 0$. Starting from a known equilibrium state denoted by $(\boldsymbol{u}_0, \ddot{\boldsymbol{u}}_0, \boldsymbol{f}_0)$, one can consider the Taylor expansion of Eq. (48), truncated at first order, considering an increment $(\Delta\boldsymbol{u}, \Delta\ddot{\boldsymbol{u}}, \Delta\boldsymbol{f})$:

$$\begin{aligned}
\boldsymbol{\varphi}_{res}(\boldsymbol{u}_0 + \Delta\boldsymbol{u}, \ddot{\boldsymbol{u}}_0 + \Delta\ddot{\boldsymbol{u}}, \boldsymbol{f}_0 + \Delta\boldsymbol{f}) &= \boldsymbol{\varphi}_{res}(\boldsymbol{u}_0, \ddot{\boldsymbol{u}}_0, \boldsymbol{f}_0) + \frac{\partial\boldsymbol{\varphi}_{res}}{\partial\boldsymbol{u}}\Delta\boldsymbol{u} + \frac{\partial\boldsymbol{\varphi}_{res}}{\partial\ddot{\boldsymbol{u}}}\Delta\ddot{\boldsymbol{u}} + \frac{\partial\boldsymbol{\varphi}_{res}}{\partial\boldsymbol{f}}\Delta\boldsymbol{f} = \\
&= \boldsymbol{\varphi}_{res}(\boldsymbol{u}_0, \ddot{\boldsymbol{u}}_0, \boldsymbol{f}_0) + \frac{\partial\mathbf{F}_{int}}{\partial\boldsymbol{u}}\Delta\boldsymbol{u} + \frac{\partial}{\partial\ddot{\boldsymbol{u}}}(\mathbf{M}\ddot{\boldsymbol{u}})\Delta\ddot{\boldsymbol{u}} - \frac{\partial\mathbf{F}_{ext}}{\partial\boldsymbol{f}}\Delta\boldsymbol{f} = \\
&= \boldsymbol{\varphi}_{res}(\boldsymbol{u}_0, \ddot{\boldsymbol{u}}_0, \boldsymbol{f}_0) + \mathbf{K}_T\Delta\boldsymbol{u} + \mathbf{M}\Delta\ddot{\boldsymbol{u}} - \mathbf{I}\Delta\lambda\boldsymbol{f}_{ref}
\end{aligned} \tag{49}$$

In Eq. (49), the linearization of the internal force term leads to the definition of the tangent stiffness matrix [49]. The linearization of the inertia load term is exploited, instead, under the assumption of a constant mass matrix. Moreover, the assumption of conservative external loads, introduced as $\boldsymbol{f} = \lambda\boldsymbol{f}_{ref}$, allows the finite variation of the external force vector to be expressed in terms of a variation of the load factor λ. The derivation of the tangent matrix in a CUF-based scenario is not reported here; the reader is referred to [49,50] for the complete procedure.

The equilibrium of the perturbed state is imposed to compute the incremental quantities required to define an equilibrium condition, thus $\boldsymbol{\varphi}_{res}(\boldsymbol{u} + \Delta\boldsymbol{u}, \ddot{\boldsymbol{u}}_0 + \Delta\ddot{\boldsymbol{u}}, \boldsymbol{f}_0 + \Delta\boldsymbol{f}) = 0$ is imposed. In this way, the final, incremental equation is rewritten as:

$$\mathbf{K}_T\Delta\boldsymbol{u} + \mathbf{M}\Delta\ddot{\boldsymbol{u}} = -\boldsymbol{\varphi}_{res}(\boldsymbol{u}_0, \ddot{\boldsymbol{u}}_0, \boldsymbol{f}_0) + \mathbf{I}\Delta\lambda\boldsymbol{f}_{ref} \tag{50}$$

The linearized problem Eq. (50) is the starting point for the definition of both the quasi-static and linearized modal problem. In the case of a quasi-static analysis, since the inertial contribution is negligible, the incremental equation is iteratively solved with a displacement-load increment constraint, to close the problem including the additional variable $\Delta\lambda$: algebraically

$$\begin{cases} \mathbf{K}_T\Delta\boldsymbol{u} = -\boldsymbol{\varphi}_{res}(\boldsymbol{u}_0, \ddot{\boldsymbol{u}}_0, \boldsymbol{f}_0) + \Delta\boldsymbol{\lambda}\boldsymbol{f}_{ref} \\ c(\Delta\boldsymbol{u}, \Delta\boldsymbol{f}) = 0 \end{cases} \tag{51}$$

The final equation is solved iteratively, depending on the constraint equation chosen, where the unbalanced nodal force vector is updated at each provisional iteration step until the increments in nodal displacements and forces satisfy the condition $\boldsymbol{\varphi}_{res}(\boldsymbol{u}, \ddot{\boldsymbol{u}}, \boldsymbol{f}) = 0$, within a predefined convergence tolerance. Typically, the path-following strategy introduced by Crisfield [51] is adopted and considered in the static nonlinear analysis. The implementation of this arc-length iterative solver within a CUF-based finite element framework has already been presented in many works; the reader is referred to [49] for more details.

In the case of linearized modal analysis around a generic non-trivial equilibrium state, the unbalanced nodal vectors contributions of Eq. (49) are disregarded. Additionally, since an undamped free vibration problem is considered, no load variations are applied; thus, $\Delta\lambda = 0$ as well. Under these conditions, considering the non-trivial equilibrium state denoted with $\mathbf{u}^k$, the governing equation for the linearized vibration problem around the configuration $\mathbf{u}^k$ is:

$$\mathbf{K}_T(\mathbf{u}^k)\Delta\boldsymbol{u}^k + \mathbf{M}\Delta\ddot{\boldsymbol{u}}^k = 0 \tag{52}$$

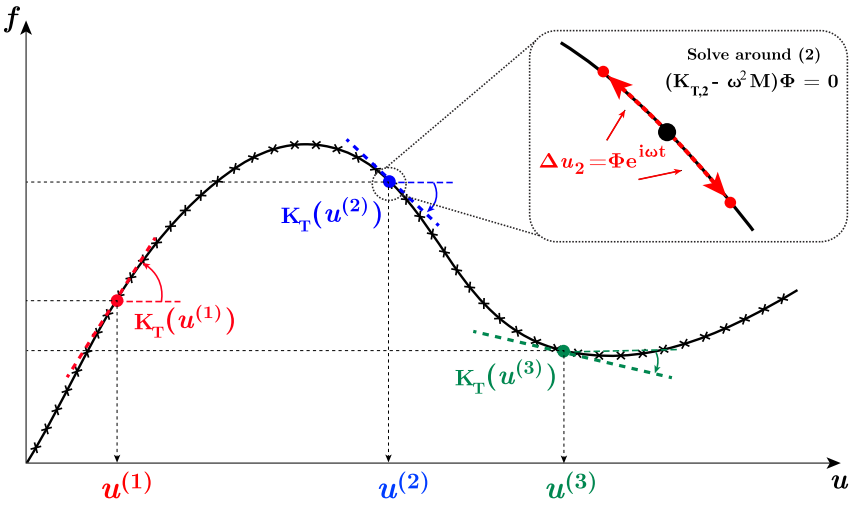

Fig. 3. Linearized vibration problem around equilibrium state: graphical interpretation.

By imposing now a generic harmonic behavior of the nodal displacement increment $\Delta \boldsymbol{u} = \boldsymbol{\Phi} e^{i\omega t}$, a linear eigenvalue problem of linearized vibrations can be defined:

$$\left(\mathbf{K}_T\left(\mathbf{u}^k\right) - \omega_k^2 \mathbf{M}\right)\boldsymbol{\Phi}^k e^{i\omega_k t} = 0 \tag{53}$$

The final equation given in Eq. (53) represents the small-amplitude free vibration problem around a non-trivial equilibrium state. After computing the tangent stiffness matrix in the chosen non-trivial equilibrium state, the linear eigenvalue problem yields the natural frequencies and modal shapes of vibration around the equilibrium state (different from the trivial one). Fig. 3 shows the geometrical representation of the algorithm presented in this work. By defining and solving Eq. (53) around each computed non-trivial equilibrium state, one can analyze the effects of pre-stressed conditions on the natural frequencies and mode shapes under large strain or large displacement [42].

The linearized terms, given by a generic finite increment of the nodal displacement vector, under the CUF formalism, are now presented briefly. In the case of internal load finite variation:

$$\begin{aligned}\Delta(\delta \mathcal{L}_{int}) &= \Delta\left(\int_{\Omega_0} \delta \boldsymbol{E}^T \boldsymbol{S} dV\right) = \int_{\Omega_0} \delta \mathbf{E}^T \Delta \mathbf{S} dV + \int_{\Omega_0} \Delta(\delta \mathbf{E}^T) \mathbf{S} dV = \\ &= \delta \boldsymbol{u}_{sj}^T \mathbf{K}_{ll}^{\tau sij} \Delta \boldsymbol{u}_{\tau i} + \delta \boldsymbol{u}_{sj}^T \mathbf{K}_{T_1}^{\tau sij} \Delta \boldsymbol{u}_{\tau i} + \delta \boldsymbol{u}_{sj}^T \mathbf{K}_{\sigma}^{\tau sij} \Delta \boldsymbol{u}_{\tau i} = \delta \boldsymbol{u}_{sj}^T \mathbf{K}_{T}^{\tau sij} \Delta \boldsymbol{u}_{\tau i}\end{aligned} \tag{54}$$

where $\mathbf{K}_{ll}^{\tau sij}$ is the FN of the linear stiffness matrix, $\mathbf{K}_{T_1}^{\tau sij}$ is the FN of the nonlinear constitutive contribution of the tangent stiffness matrix, and $\mathbf{K}_{\sigma}^{\tau sij}$ is the FN of the geometric stiffness matrix. Considering the summation over the indices and CUF assembling procedure, as previously addressed, the second term of Eq. (49) is obtained. The complete derivation of the analytic expression of the tangent stiffness matrix FN for hyperelastic materials can be found in Pagani and Carrera [52].

The linearized form of the inertial contribution of the variational principle is exploited again through the hypothesis of the constant mass matrix, considering the same derivation procedure, by a Taylor expansion truncated at the first order around a known equilibrium condition:

$$\Delta(\delta \mathcal{L}_{ine}) = \Delta(\delta \boldsymbol{u}_{sj}^T \mathbf{M}^{\tau sij} \ddot{\boldsymbol{u}}_{\tau i}) = \delta \boldsymbol{u}_{sj}^T \Delta \mathbf{M}^{\tau sij} \ddot{\boldsymbol{u}}_{\tau i} + \delta \boldsymbol{u}_{sj}^T \mathbf{M}^{\tau sij} \Delta \ddot{\boldsymbol{u}}_{\tau i} = \delta \boldsymbol{u}_{sj}^T \mathbf{M}^{\tau sij} \Delta \ddot{\boldsymbol{u}}_{\tau i} \tag{55}$$

5. Numerical results

This section presents several case studies and numerical results for the static and linearized modal analysis of fiber-reinforced hyperelastic materials and biological tissues. The analyses are performed using the current implementation of higher-order models, which enhances the capabilities of the proposed approach in terms of hyperelastic constitutive modeling and the inclusion of anisotropic effects in the model. The results are compared against reference solutions obtained from conventional 3D finite element models implemented in ABAQUS.

5.1. Circular plate under large displacements

In the first case, the static and modal analysis of a clamped circular plate made of fiber-reinforced hyperelastic materials is performed. This case study has been proposed by Beheshti et al. [53] and further investigated by the authors in Chiaia et al. [38]. A

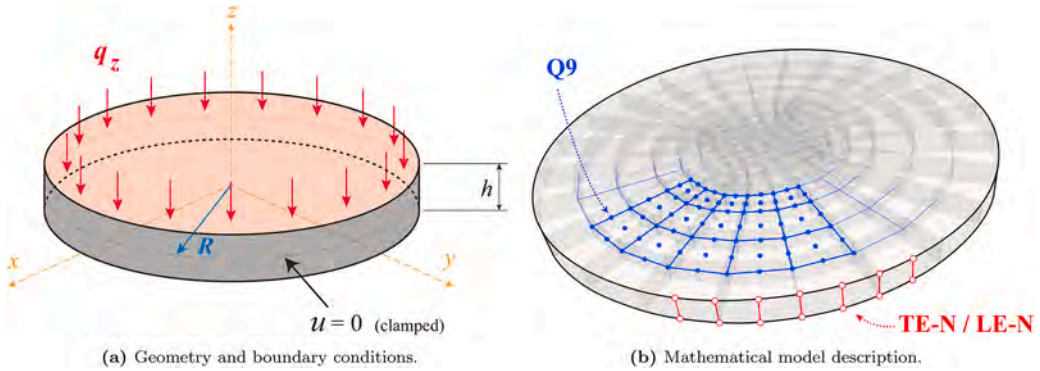

Fig. 4. Compressible circular plate: configuration of the case study and discretization adopted.

clamped circular plate of radius $R = 50$ mm and thickness $h = 5$ mm is subjected to a vertical transversal pressure q_z. The plate is made of a compressible, reinforced material, with a single family of fibers given by $\boldsymbol{a}_0$. Two different fiber-reinforcement configurations are considered: radial and tangential (circumferential) fiber distributions. The geometrical features and the boundary conditions applied are represented in Fig. 4.

The material model considered is given by [53] and exploits a simple quadratic model for the fiber-reinforcement term:

$$\Psi(\mathbf{C}) = \frac{\mu}{2}(I_1 - 3) + \frac{\lambda}{2}(J-1)^2 - \mu \log J + \gamma(I_4 - 1)^2 \tag{56}$$

considering $\mu = 1$ MPa, $\lambda = 4$ MPa and $\gamma = 0.375$ MPa. The objective of the proposed analysis is to investigate the influence of fiber orientation on the pure mechanical response of the structure, while also analyzing the impact of through-the-thickness discretization. In the following, higher-order 2D plate models will be adopted for the discretization of the circular plate, considering the assessment of the proposed methodology in Chiaia et al. [38], where the effectiveness of the 2D plate CUF model has been discussed. First, a nonlinear static analysis is performed for both fiber distributions, measuring the vertical transverse displacement u_z at the center of the plate, and comparing the results with the available reference. The equilibrium paths, presented in Fig. 5, are obtained using an already validated discretization model adopting 180 Q9 parabolic elements along the reference mid-surface, as analyzed in Chiaia et al. [38]. The influence of the structural theory approximation is assessed by comparing results from two thickness expansion models: one using a parabolic (LE2) model and the other a cubic (LE3) model. In both fiber configurations, the numerical results proposed are in excellent agreement with the reference. Slight discrepancies are observed under extreme conditions in the radial fiber case, where the CUF 2D model exhibits a softer response. However, a global relative error of 1.24% in the computed solution has been observed at $q_z = 0.1$ MPa.

Thereafter, in each computed (and marked in the equilibrium path) non-trivial equilibrium state, the linear eigenvalue problem is solved, evaluating then the natural frequencies and mode shapes around different deformed configurations. Fig. 6 illustrates the pressure-frequency curve of the first ten natural frequencies along the equilibrium path for the radial fiber distribution, comparing the results obtained for different CUF expansion models. A similar comparison is conducted for the tangential fiber distribution case and presented in Fig. 7.

From the proposed results, different modal interactions are observed in both the small- and large-displacement regimes. In particular, both for radial and tangential fiber distribution cases, modal interactions are observed for high-frequency modes. To investigate the behavior of modal shapes in interacting zones, different criteria can be adopted. Here, the mode shapes for the tangential distribution case are analyzed. From the pressure-frequency results shown in Fig. 7, modal interactions between modes eight, nine, and ten are observed as the applied pressure increases, unlike the first six natural frequencies, where modal interactions are only slightly observed at extremely deformed configurations. Fig. 8 shows the eight modes of vibration, computed in different non-trivial equilibrium states. The same comparison is proposed for the ninth mode of vibration in Fig. 9. From the pressure-frequency curve of the tangential distribution case, an evident modal interaction can be observed between modes 8 and 9, around the condition $q_z = 0.064$ MPa. In particular, a crossing between normal modes of vibration is observed, where the flexural eight mode of vibration is swapped with the torsional ninth mode. The same investigation is conducted for the non-trivial equilibrium state near the condition $q_z = 0.020$ MPa, where the interaction between modes eight-nine and the tenth mode is observed. Fig. 10 shows the variation of the eight vibration modes in different non-trivial equilibrium states. The same representation is proposed in Fig. 11 for the tenth mode shape of vibration. In fact, a pure bending/flexural mode is interacting with a flexural/volumetric mode, and again crossing between normal modes of vibration can be observed. The results suggest that, for a radial fiber configuration, the plate exhibits stiffer behavior, as confirmed by the linearized vibration analysis, which shows higher natural frequencies across all cases. On the other hand, more evident modal interactions instead are observed in the case of tangential fiber distribution. These preliminary results constitute an assessment of the proposed procedure, further motivating investigations into the influence of prestressed conditions on the dynamic and modal analysis of structures.

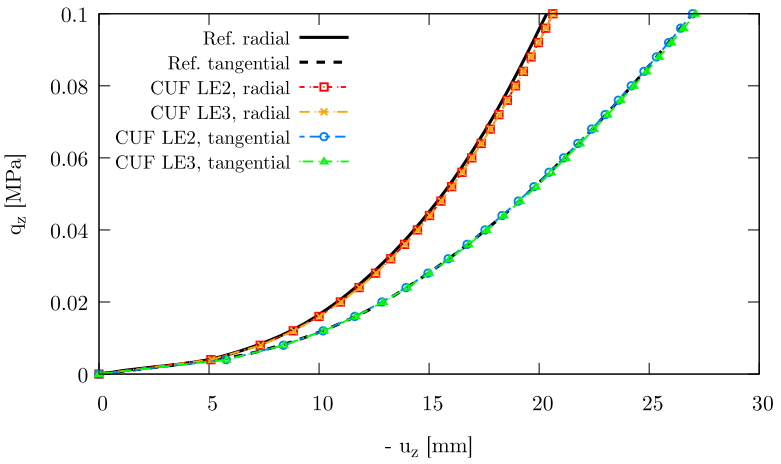

Fig. 5. Equilibrium path of the compressible circular plate.

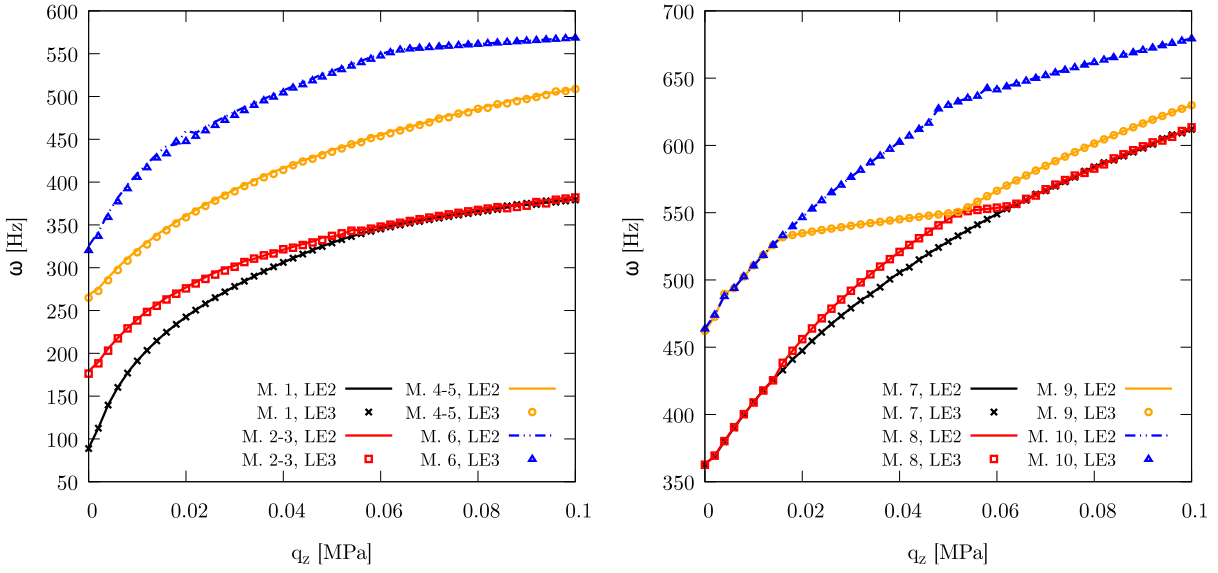

(a) Modes 1-6 **(b)** Modes 7-10

Fig. 6. Variation of the first ten natural frequencies along the equilibrium path. Compressible circular plate; radial fiber configuration.

5.2. Effects of large displacements on biological tissue multilayered specimen

In this section, a numerical model for a multilayered plate composed of iliac adventitial strips, as considered in Gasser et al. [11], is presented. In this strain energy function model, as in the reference, at least three distinct microstructural phases can be observed and modeled independently: an isotropic ground matrix and two fiber families. A biological-like cantilever plate is analyzed, considering the effect of the fiber dispersion and orientation on the static and dynamic response of the structure. The strain energy function model adopted in the following is the Holzapfel-Gasser-Ogden (HGO) potential without any tension/compression model included:

$$\Psi = \frac{K}{2}\left(\frac{J^2-1}{2} - \log J\right) + \frac{\mu}{2}(\bar{I}_1 - 3) + \sum_{j=4,6} \frac{k_1}{2k_2}\left[e^{k_2(k\bar{I}_1+(1-3k)\bar{I}_j-1)^2} - 1\right] \tag{57}$$

where μ is the initial shear modulus of the isotropic Neo-Hookean ground matrix, k_1 and k_2 are material constants calibrated from experimental data, K is the material bulk modulus, and k is the fiber dispersion parameter. In the proposed case study, a rectangular plate with equal thickness $h_l = 1$ mm is considered, with base dimensions $a = 100$ mm and $b = 50$ mm. The geometrical features are depicted in Fig. 12(a). The material constants are described in [11] considering an aortic iliac material, for which $\mu = 7.64$ kPa, $k_1 = 996.6$ kPa, $k_2 = 524.6$, and $K = 38.147$ MPa, considering then a typical density value of $\rho = 1300\, kg/m^3$. Given the chosen value of

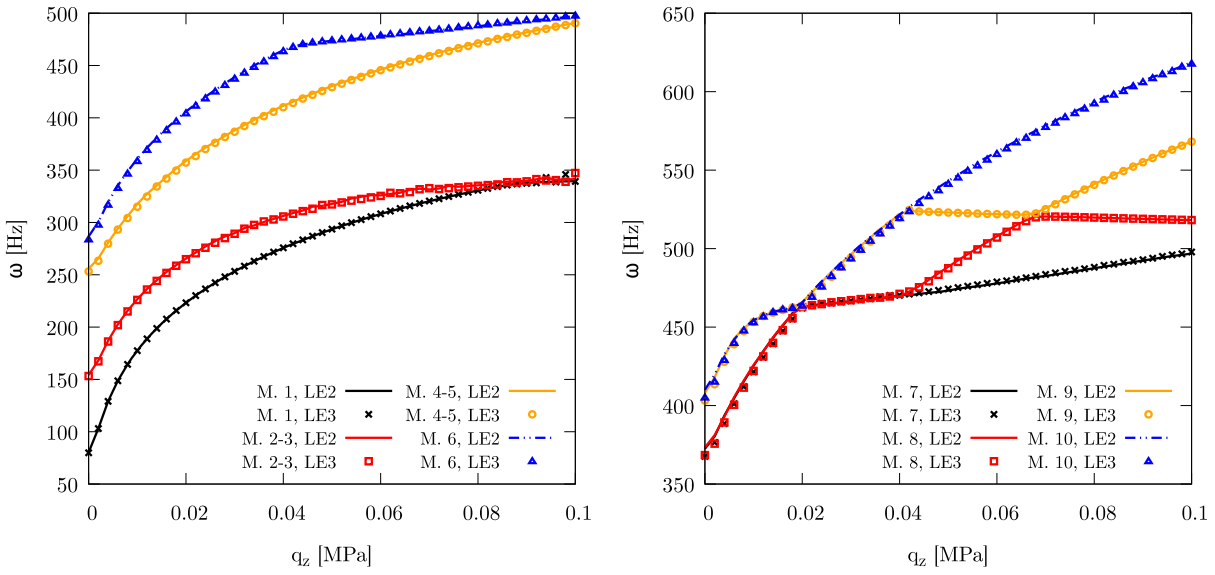

(a) Modes 1-6 **(b)** Modes 7-10

Fig. 7. Variation of the first ten natural frequencies along the equilibrium path. Compressible circular plate; tangential fiber configuration.

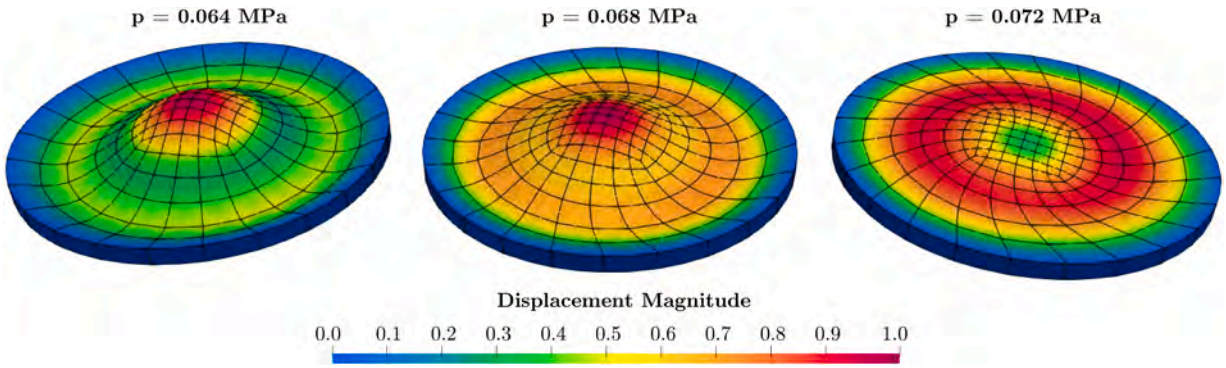

Fig. 8. Eight mode of vibration for different deformed configurations. Compressible circular plate; tangential fiber configuration. Eigenvalue represented on the undeformed configuration.

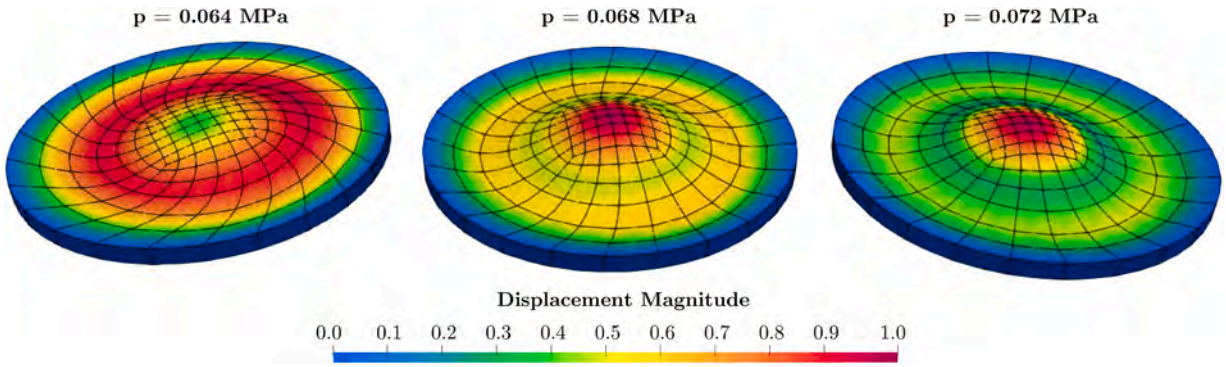

Fig. 9. Ninth mode of vibration for different deformed configurations. Compressible circular plate; tangential fiber configuration. Eigenvalue represented on the undeformed configuration.

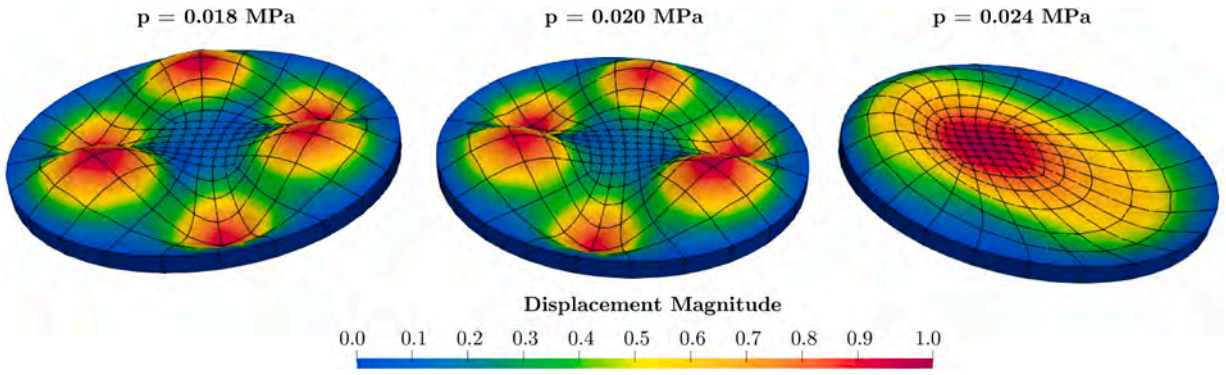

Fig. 10. Eight mode of vibration for different deformed configurations. Compressible circular plate; tangential fiber configuration. Eigenvalue represented on the undeformed configuration.

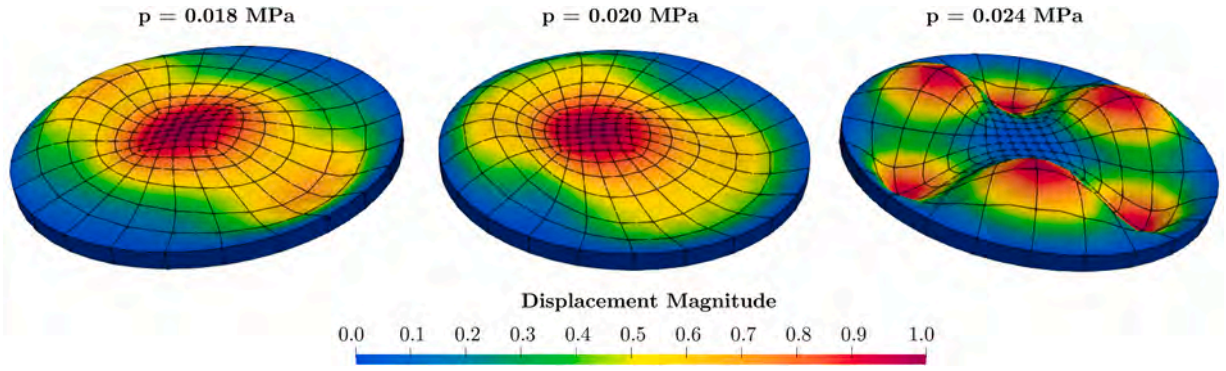

Fig. 11. Tenth mode of vibration for different deformed configurations. Compressible circular plate; tangential fiber configuration. Eigenvalue represented on the undeformed configuration.

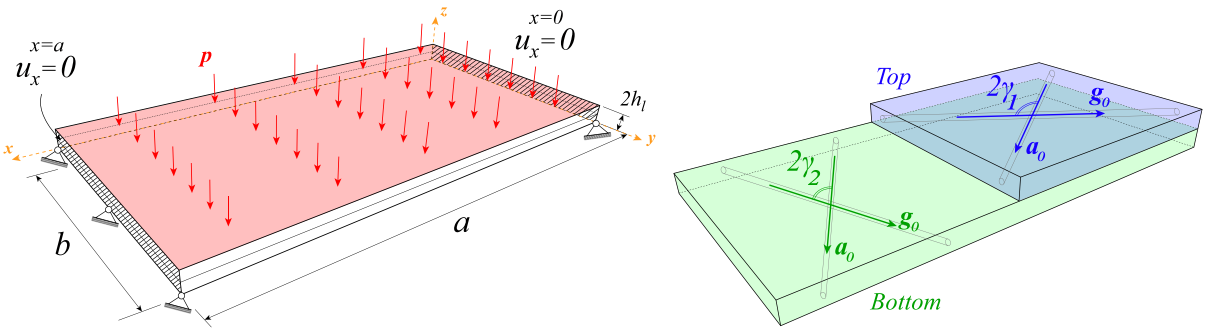

(a) Geometry and boundary conditions. **(b)** Fibre distributions considered.

Fig. 12. Biological multilayered plate: geometrical and material features considered.

K, the initial Poisson ratio is $\nu = 0.4999$, thus modeling the biological plate in the nearly incompressible regime. The plate of fibrous soft tissues is considered with fibers oriented in the $x - y$ plane with opening angles $\gamma_1 = 45°$ and $\gamma_2 = 30°$, as shown in Fig. 12(b).

The capabilities of the present methodology are discussed by analyzing the static, modal, and non-trivial linearized vibration response of the plate. Specifically, to avoid the mathematical inconsistency of the built-in HGO model in extremely deformed states, a `UANISOHYPER_INV` subroutine has been developed, where the strain energy function Eq. (57) and its derivatives are included, as discussed in Fehervary et al. [54]. In this way, it is possible to simulate any fiber-reinforced material model within the ABAQUS commercial software. The results obtained with high-order 2D CUF models are compared with a reference solution from 3D hexahedral FEM models, and the proposed equilibrium paths are compared with the load-displacement results from fully 3D solutions. The ABAQUS model adopts 13,924 C3D20 (20-node brick elements, parabolic model). In the first case, the modal behavior of the plate is analyzed considering the free vibration problem around the trivial undeformed equilibrium state. The plate is studied under two different conditions: dispersed fibers ($k = 0.226$) and perfectly aligned fibers ($k = 0$), for both layers. Furthermore, the nonlinear static

Table 1
Convergence analysis for the first ten natural frequencies [Hz]. Biological multilayered plate, dispersed fiber case $k = 0.226$. Comparison between high-order 2D CUF models and 3D ABAQUS reference solution. In brackets, the percentage difference with respect to ABAQUS is given.

	Parabolic expansion per layer (1 LE2)				Cubic expansion per layer (1 LE3)				ABQ 3D
Mode	Model A 10×10 Q9	Model C 10×15 Q9	Model E 15×20 Q9	Model G 20×20 Q9	Model B 10×10 Q9	Model D 10×15 Q9	Model F 15×20 Q9	Model H 20×20 Q9	C3D20
1	1.667(1.66%)	1.651(0.68%)	1.645(0.35%)	1.645(0.33%)	1.662(1.35%)	1.646(0.36%)	1.640(0.01%)	1.640(0.00%)	1.640
2	4.612(2.69%)	4.531(0.87%)	4.510(0.40%)	4.509(0.38%)	4.596(2.32%)	4.514(0.50%)	4.493(0.02%)	4.492(0.01%)	4.492
3	4.920(0.91%)	4.899(0.49%)	4.890(0.31%)	4.890(0.30%)	4.899(0.48%)	4.877(0.03%)	4.868(0.16%)	4.867(0.17%)	4.875
4	9.223(4.17%)	8.954(1.12%)	8.895(0.46%)	8.893(0.44%)	9.183(3.72%)	8.913(0.66%)	8.855(0.01%)	8.853(0.01%)	8.854
5	10.025(1.20%)	9.962(0.57%)	9.939(0.33%)	9.938(0.32%)	9.974(0.69%)	9.909(0.03%)	9.886(0.21%)	9.884(0.22%)	9.906
6	15.071(2.47%)	14.933(1.53%)	14.795(0.59%)	14.790(0.56%)	14.994(1.95%)	14.845(0.93%)	14.708(0.00%)	14.704(0.03%)	14.708
7	15.522(3.34%)	15.053(0.22%)	15.041(0.14%)	15.040(0.13%)	15.555(3.56%)	14.973(0.31%)	14.959(0.41%)	14.958(0.42%)	15.020
8	15.641(2.67%)	15.344(0.72%)	15.293(0.38%)	15.291(0.37%)	15.430(1.28%)	15.248(0.08%)	15.196(0.26%)	15.194(0.27%)	15.235
9	19.683(1.00%)	19.604(0.60%)	19.570(0.42%)	19.568(0.41%)	19.528(0.21%)	19.439(0.25%)	19.400(0.45%)	19.398(0.46%)	19.488
10	21.727(3.42%)	21.228(1.05%)	21.111(0.49%)	21.106(0.47%)	21.576(2.70%)	21.072(0.30%)	20.954(0.26%)	20.949(0.28%)	21.008
DOFs	6615	9765	19,065	25,215	9261	13,671	26,691	35,301	234,009

Table 2
Convergence analysis for the first ten natural frequencies [Hz]. Biological multilayered plate, perfectly aligned fiber case $k = 0$. Comparison between high-order 2D CUF models and 3D ABAQUS reference solution.In brackets, the percentage difference with respect to ABAQUS is given.

	Parabolic expansion per layer (1 LE2)				Cubic expansion per layer (1 LE3)				ABQ 3D
Mode	Model A 10×10 Q9	Model C 10×15 Q9	Model E 15×20 Q9	Model G 20×20 Q9	Model B 10×10 Q9	Model D 10×15 Q9	Model F 15×20 Q9	Model H 20×20 Q9	C3D20
1	3.283(1.75%)	3.255(0.89%)	3.243(0.54%)	3.243(0.52%)	3.222(0.12%)	3.191(1.08%)	3.178(1.47%)	3.178(1.49%)	3.226
2	8.630(1.96%)	8.536(0.86%)	8.506(0.50%)	8.505(0.49%)	8.477(0.16%)	8.376(1.03%)	8.344(1.41%)	8.343(1.42%)	8.464
3	10.295(0.99%)	10.257(0.62%)	10.239(0.44%)	10.238(0.43%)	10.150(0.43%)	10.109(0.84%)	10.091(1.02%)	10.090(1.02%)	10.194
4	16.534(2.55%)	16.253(0.81%)	16.187(0.40%)	16.185(0.38%)	16.217(0.58%)	15.918(1.27%)	15.848(1.70%)	15.847(1.71%)	16.123
5	19.917(0.87%)	19.845(0.51%)	19.813(0.34%)	19.812(0.34%)	19.654(0.46%)	19.578(0.84%)	19.548(1.00%)	19.547(1.00%)	19.745
6	27.299(3.23%)	26.674(0.86%)	26.544(0.37%)	26.540(0.36%)	26.778(1.25%)	26.113(1.26%)	25.975(1.78%)	25.972(1.79%)	26.446
7	28.436(1.01%)	28.291(0.49%)	28.240(0.31%)	28.238(0.31%)	28.057(0.34%)	27.910(0.86%)	27.861(1.03%)	27.860(1.04%)	28.152
8	31.812(0.09%)	31.799(0.05%)	31.791(0.03%)	31.790(0.02%)	31.360(1.33%)	31.342(1.39%)	31.331(1.42%)	31.331(1.42%)	31.783
9	33.549(0.86%)	33.448(0.56%)	33.397(0.40%)	33.394(0.39%)	32.900(1.09%)	32.785(1.44%)	32.731(1.60%)	32.729(1.61%)	33.263
10	36.249(1.76%)	35.841(0.61%)	35.739(0.32%)	35.736(0.31%)	35.751(0.36%)	35.344(0.78%)	35.245(1.06%)	35.243(1.07%)	35.624
DOFs	6615	9765	19,065	25,215	9261	13,671	26,691	35,301	234,009

analysis of the two plates is performed using the same discretization and expansion models as for the free vibration analysis to assess the influence of both the reference mid-surface discretization model and the through-the-thickness kinematics on the mechanical response. The accuracy and the efficiency of the present model are measured by comparing the results adopting the relative percentage difference between solutions and the total number of DOF required by the simulation, respectively. Table 1 shows the convergence analysis performed considering the dispersed fiber distribution case, for which $k = 0.226$, analyzing the influence of the mid-surface discretization and theory of structure approximation regarding the first ten natural frequencies. The relative percentage difference between 2D CUF models and reference solutions obtained using ABAQUS commercial software is reported in brackets. The same comparison is proposed in Table 2 regarding the case of perfectly aligned fiber ($k = 0$). Also, from the proposed results and for both material conditions considered, a significant reduction in DOF for the computation of accurate natural frequencies is observed, up to around 8% of the DOF required by the ABAQUS convergent mesh (taking model E as reference). These proposed models are now discussed in terms of static nonlinear analysis.

Fig. 13(a) depicts the plate equilibrium path for dispersed fibers ($k = 0.226$). The global load-displacement curve is again compared with the numerical reference solution obtained from fully 3D models. The same comparison is proposed in the case of perfectly aligned fibers ($k = 0$) in Fig. 13(b). The results of the static nonlinear analysis serve as the starting point for the subsequent modal analysis. For each computed nontrivial equilibrium state, the linearized vibration problem is defined and solved for both fiber dispersion configurations. Fig. 14 depicts the pressure-frequencies curve in the case of dispersed fiber $k = 0.226$, in the small displacement regime. Specifically, the variation of the first four natural frequencies, obtained by the previously listed FE discretization, is proposed in Fig. 14(a), and (b) proposes the same comparison for the second four natural frequencies (modes five to eight). The same results are depicted in Fig. 15 for the entire computed equilibrium path, illustrating the modal interaction in the large strain regime for the multilayered biological plate with dispersed fibers.

Fig. 16 shows, using the $20\times20+1$LE2 model, a comparison between the computed pressure-frequency curve and results from fully 3D ABAQUS models. In particular, Fig. 16(a) depicts the comparison between 2D CUF and 3D ABAQUS results in terms of the first ten natural frequencies, obtained in different non-trivial equilibrium states, instead Fig. 16(b) shows the global behavior of the first ten normal modes of vibration. From the latter, it is possible to observe different modal interactions at small and large strains.

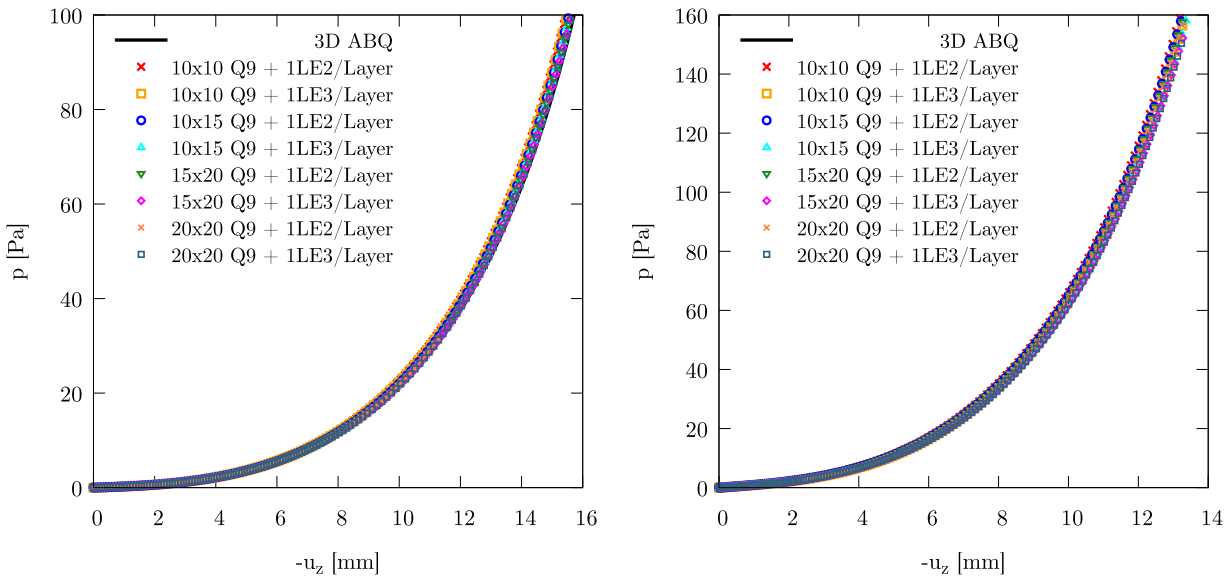

(a) $k = 0.226$ **(b)** $k = 0$

Fig. 13. Equilibrium paths obtained of the simply supported biological multilayered plate subjected to uniform traction pressure. Comparison between high-order 2D CUF models and 3D ABAQUS reference solution.

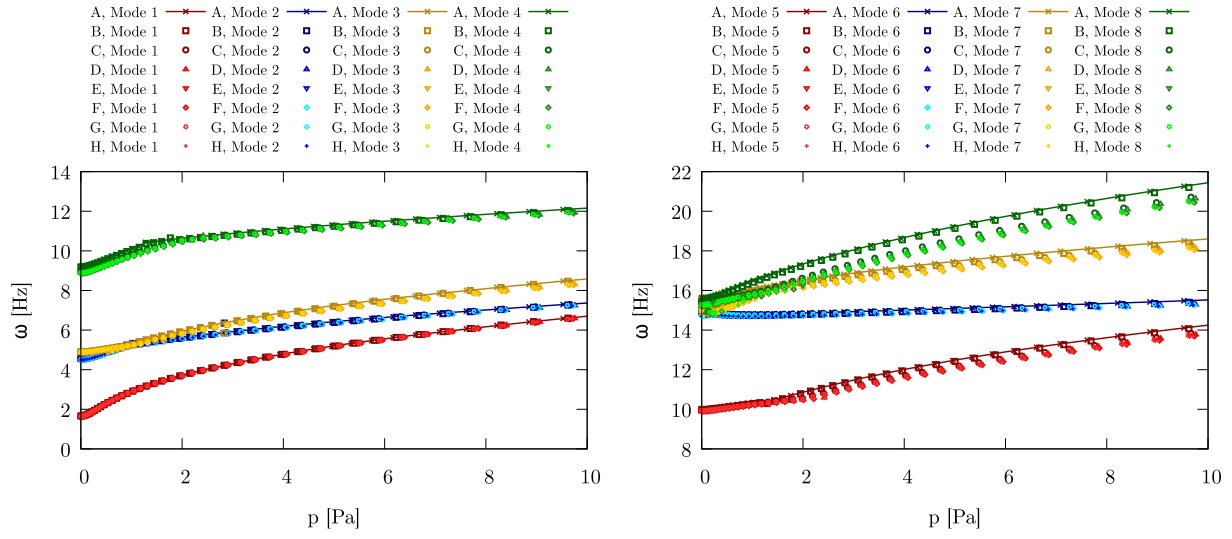

(a) Modes 1-4 **(b)** Modes 5-8

Fig. 14. Variation of the first eight natural frequencies of the biological multilayered plate ($k = 0.226$) along the equilibrium path, small strain regime. Influence of structural theory and reference mid-surface discretization.

These interactions are further investigated through the Modal Assurance Criterion (MAC), a correlation measure that compares different sets of eigenvectors and thus examines the correlation between mode shapes. In general, the sets A and B of eigenvectors, the MAC matrix comparing these two sets is defined:

$$MAC_{ij} = \frac{\left|\boldsymbol{\Phi}_{A_i}^T \boldsymbol{\Phi}_{B_j}\right|^2}{\left(\boldsymbol{\Phi}_{A_i}^T \boldsymbol{\Phi}_{A_i}\right)\left(\boldsymbol{\Phi}_{B_j}^T \boldsymbol{\Phi}_{B_j}\right)} \tag{58}$$

Fig. 17 shows different MAC matrices, comparing the normal modes of vibration of the undeformed reference state with the linearized vibration solutions around different deformed configurations. The deformed state is indicated in the caption. From the proposed result,

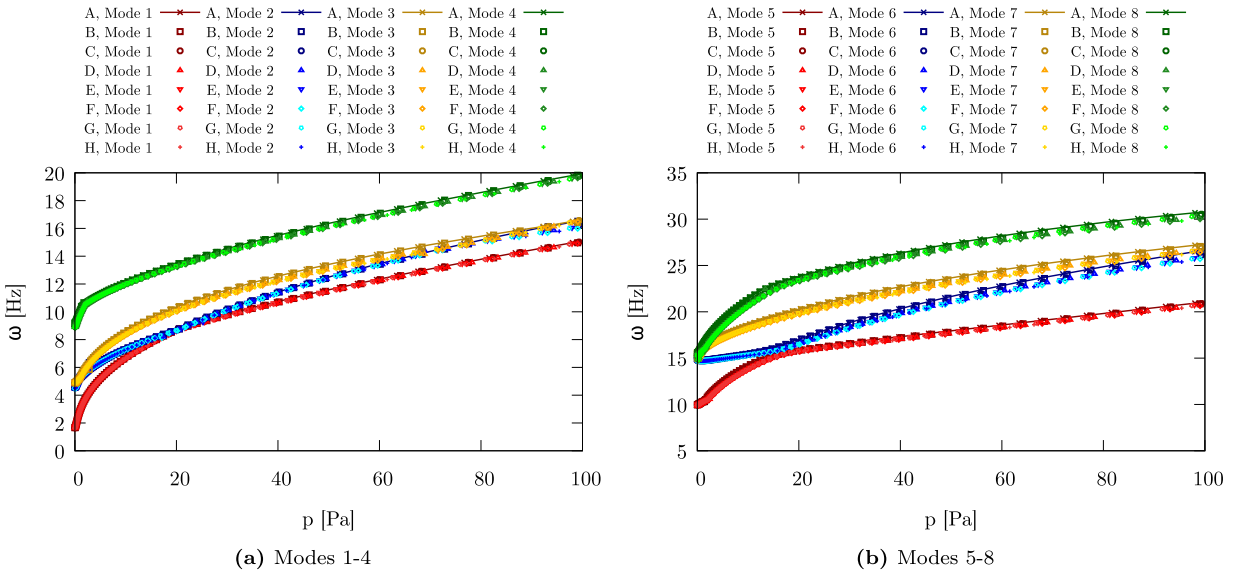

(a) Modes 1-4 **(b)** Modes 5-8

Fig. 15. Variation of the first eight natural frequencies of the biological multilayered plate ($k = 0.226$) along the equilibrium path, large strain regime. Influence of structural theory and reference mid-surface discretization.

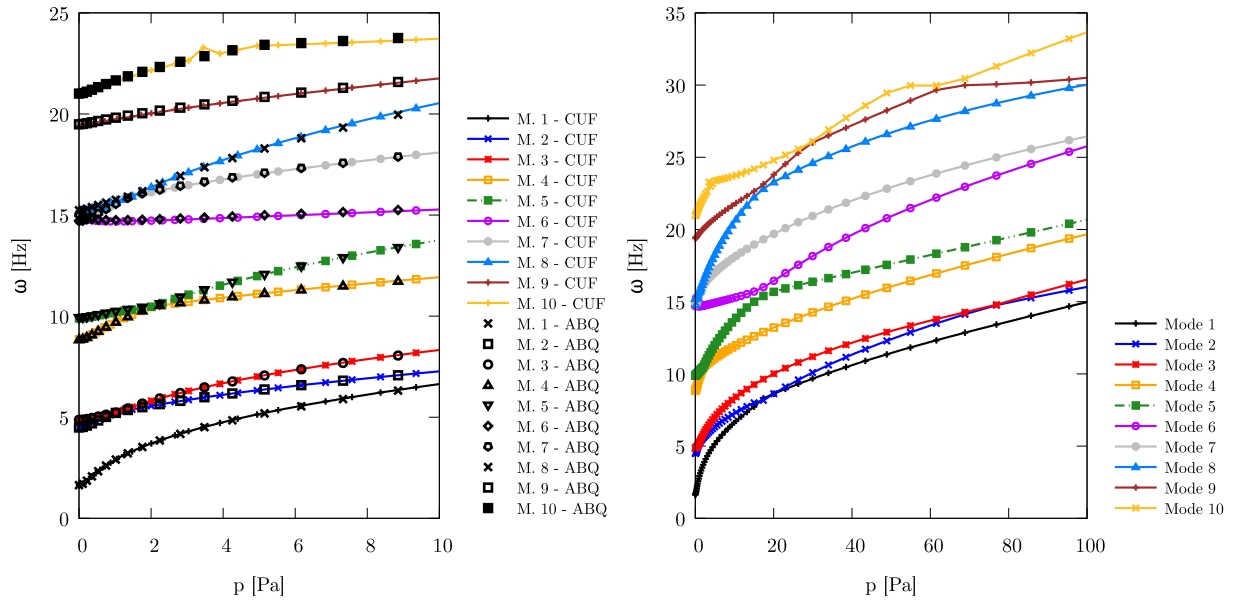

(a) Small strain regime **(b)** Global strain regime

Fig. 16. Variation of the first ten natural frequencies of the biological multilayered plate ($k = 0.226$) along the equilibrium path. Comparison between high-order 2D CUF models and 3D ABAQUS reference solution.

one can observe that, for slightly deformed configurations in the small-strain regime, normal modes of vibration do not interact, and specifically swapping and crossing are observed. Instead, in the case of large strain, more evident modal interactions are observed, as the case of mode 4-5 followed in Fig. 17(b). To characterize the modal interaction, the specific normal modes of vibration are depicted in Fig. 18. From the modal shapes, one can observe a veering phenomenon, in which the normal modes of vibration interact without preserving their previous characteristics; thus, different modal shapes arise. The two solution paths of the fifth and sixth modes exhibited smooth behavior until a proximity condition was reached, around $p = 18$ Pa. Here, rather than intersecting continuously, the two frequency-pressure curves underwent an avoided crossing, each deflecting following the path that the other curve would have followed [55].

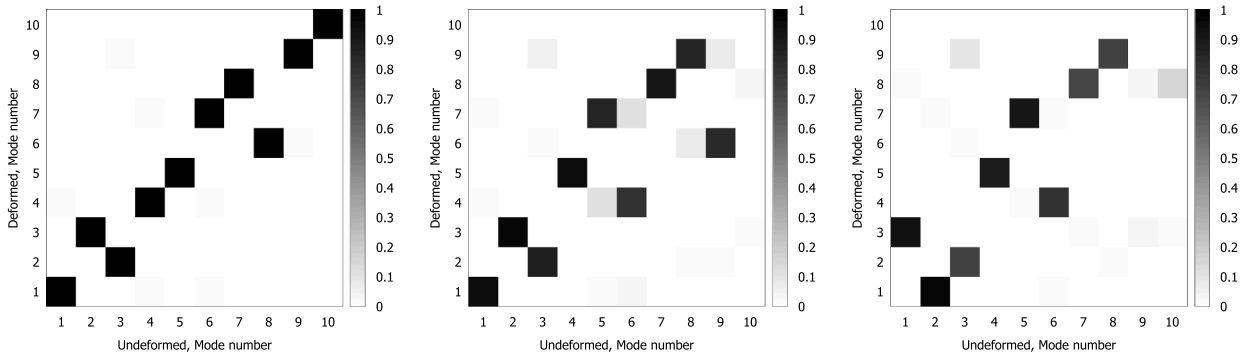

(a) $p = 1.38$ Pa (b) $p = 21.44$ Pa (c) $p = 73.18$ Pa

Fig. 17. MAC matrix computed comparing the undeformed modal shapes with respect to different deformed configuration modal shapes. Biological multilayered plate, $k = 0.226$ case. The deformed configuration state is indicated in the sub-caption.

Table 3
Convergence analysis for the first three natural frequencies [Hz]. Large strain analysis of an aortic iliac strip, cases $k = 0.226$ and $k = 0$. Comparison between high-order 1D model results and 3D ABAQUS solution. In brackets, the percentage difference with respect to ABAQUS is given.

		Dispersed fibers $\mathbf{k} = 0.226$			Perfectly aligned fibers $\mathbf{k} = 0$			
Mesh	Exp.	Mode 1	Mode 2	Mode 3	Mode 1	Mode 2	Mode 3	DOF
10 B4	16 L9	$89.329^{(1.76\%)}$	$184.508^{(1.02\%)}$	$204.205^{(1.19\%)}$	$106.305^{(1.55\%)}$	$201.683^{(-0.33\%)}$	$276.915^{(2.99\%)}$	7533
	24 L9	$89.342^{(1.77\%)}$	$185.028^{(1.30\%)}$	$204.137^{(1.15\%)}$	$105.810^{(1.08\%)}$	$202.003^{(-0.17\%)}$	$272.986^{(1.53\%)}$	11,067
	35 L9	$89.112^{(1.51\%)}$	$184.141^{(0.82\%)}$	$203.749^{(0.96\%)}$	$105.457^{(0.74\%)}$	$201.105^{(-0.62\%)}$	$272.247^{(1.25\%)}$	15,345
15 B4	16 L9	$88.732^{(1.08\%)}$	$183.903^{(0.69\%)}$	$203.340^{(0.76\%)}$	$105.990^{(1.25\%)}$	$201.541^{(-0.40\%)}$	$275.452^{(2.44\%)}$	11,178
	24 L9	$88.704^{(1.04\%)}$	$184.437^{(0.98\%)}$	$203.175^{(0.68\%)}$	$105.337^{(0.63\%)}$	$201.872^{(-0.24\%)}$	$270.658^{(0.66\%)}$	16,422
	35 L9	$88.467^{(0.77\%)}$	$183.503^{(0.47\%)}$	$202.782^{(0.48\%)}$	$105.013^{(0.32\%)}$	$200.946^{(-0.70\%)}$	$270.106^{(0.46\%)}$	22,270
20 B4	16 L9	$88.455^{(0.76\%)}$	$183.628^{(0.54\%)}$	$202.963^{(0.57\%)}$	$105.847^{(1.11\%)}$	$201.480^{(-0.43\%)}$	$274.776^{(2.19\%)}$	14,823
	24 L9	$88.404^{(0.70\%)}$	$184.166^{(0.83\%)}$	$202.751^{(0.47\%)}$	$105.150^{(0.45\%)}$	$201.816^{(-0.27\%)}$	$269.800^{(0.34\%)}$	21,777
	35 L9	$88.166^{(0.43\%)}$	$183.210^{(0.31\%)}$	$202.359^{(0.27\%)}$	$104.839^{(0.15\%)}$	$200.878^{(-0.73\%)}$	$269.322^{(0.16\%)}$	30,195
ABQ	6734 C3D20	87.788	182.650	201.810	104.681	202.354	268.882	95,514

Afterwards, the same linearized vibration analysis is performed for the perfectly aligned ($k = 0$) fiber case. Fig. 19 depicts the pressure-frequencies curve in the case of aligned fiber $k = 0$, in the small displacement regime. Specifically, the variation of the first four natural frequencies, obtained by the previously listed FE discretization, is proposed in Fig. 19(a). Fig. 19(b) proposes the same comparison for the second four natural frequencies (modes five to eight). The same results are depicted in Fig. 20 for the entire computed equilibrium path, showing the modal interaction in the large-strain regime for the multilayered biological plate with perfectly aligned fibers.

Fig. 21 shows, again adopting the $20 \times 20 + 1$ LE2 model, a comparison between the computed pressure-frequency curve and results from fully 3D models implemented in ABAQUS. In particular, Fig. 21(a) depicts the comparison between 2D CUF and 3D ABAQUS results in terms of the first ten natural frequencies, obtained in different non-trivial equilibrium states, instead Fig. 21(b) shows the global behavior of the first ten normal modes of vibration. From the latter, it is possible to observe different modal interactions at small and large strains. A perfect match between solutions across modes is observed when compared with the reference 3D ABAQUS results, demonstrating the accuracy and the capabilities of the present high-order model to capture the effects of nonlinearities on the linearized vibration behavior of anisotropic hyperelastic materials.

Modal interactions are again analyzed using the MAC matrix. Fig. 22 shows different MAC matrices, comparing the normal modes of vibration of the undeformed reference state with the linearized solutions obtained around different deformed configurations. The deformed state is indicated in the caption. From the proposed result, one can observe that, for slightly deformed configurations in the small-strain regime, normal modes of vibration do not interact, and specifically swapping and crossing are observed. Instead, in the case of large strain, more evident modal interactions are observed, as the case of mode 4–5 observed in Fig. 22(b). Higher natural frequencies are associated with dispersed fibers and with the modal interaction mechanism. In particular, comparing the results proposed in Fig. 21(b) with respect to the dispersed fiber case depicted in Fig. 16(b), the observed modal interactions are measured at relatively higher loads. The performed investigation about modal interaction is proposed here again, for the case of the fifth and sixth modes of vibration, around the condition $p = 85$ Pa. Fig. 23(a) shows the comparison between the fifth mode of vibration evaluated at $p = 83.64$ Pa and $p = 92.89$ Pa. A similar comparison is proposed in Fig. 23(b) for the sixth mode of vibration. In the case of modal shapes, unlike the case of dispersed fibers, one can observe a crossing phenomenon, where the normal modes of vibration interact without changing the modal shapes. The two solution paths follow the path that the other curve would have followed before the crossing, but the mode shapes are not interacting [55].

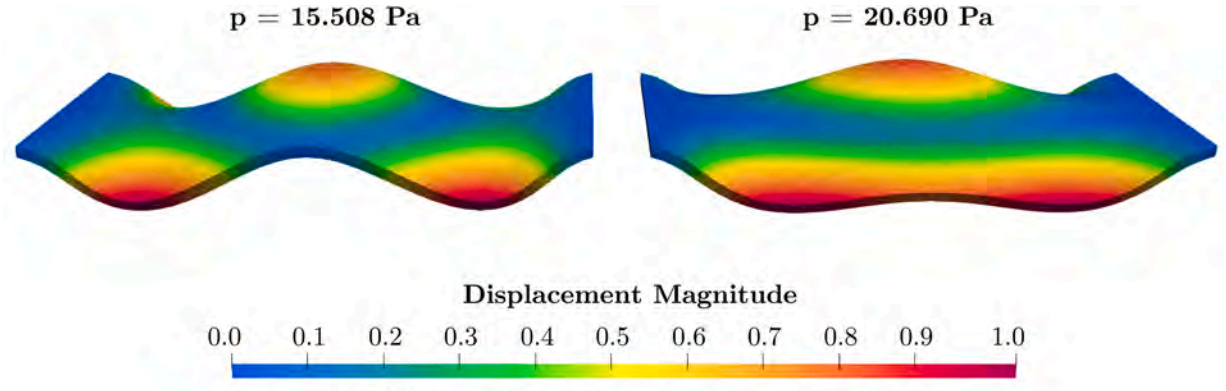

(a) Mode 5, for the two indicated deformed configurations

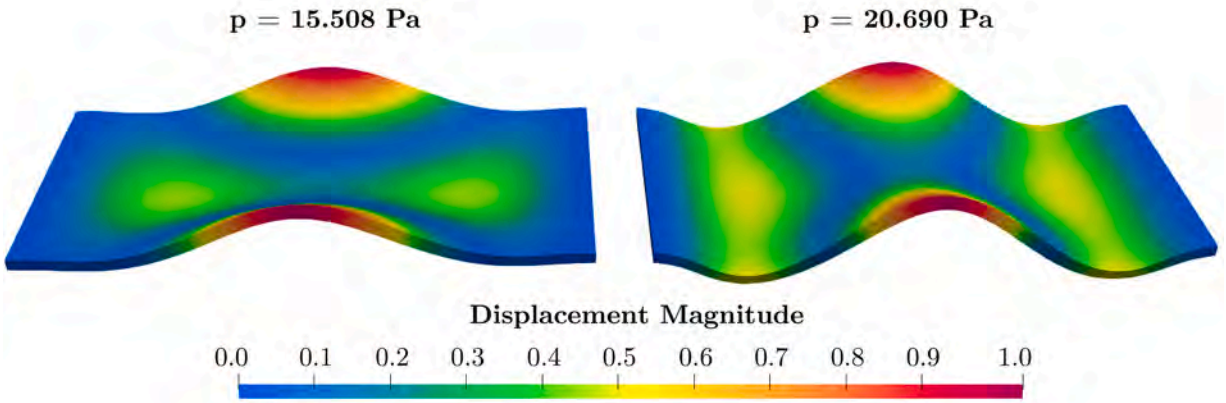

(b) Mode 6, for the two indicated deformed configurations

Fig. 18. Eigenvector representation on the undeformed structures, modes 5 and 6, veering observed. Biological multilayered plate, $k = 0.226$ case.

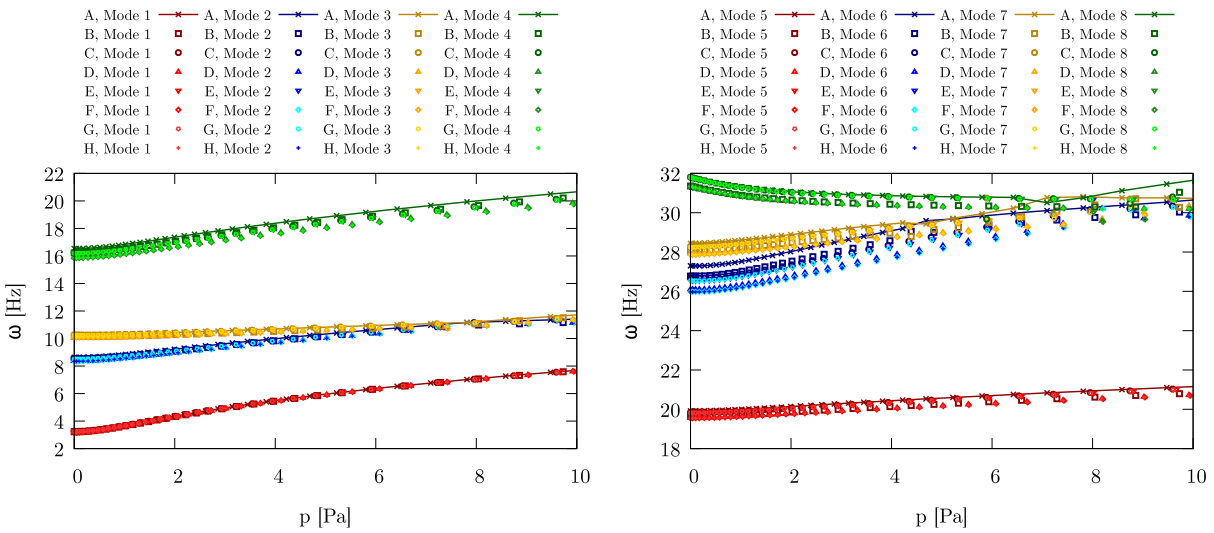

(a) Modes 1-4 (b) Modes 5-8

Fig. 19. Variation of the first eight natural frequencies of the biological multilayered plate ($k = 0$) along the equilibrium path, small strain regime. Influence of structural theory and reference mid-surface discretization.

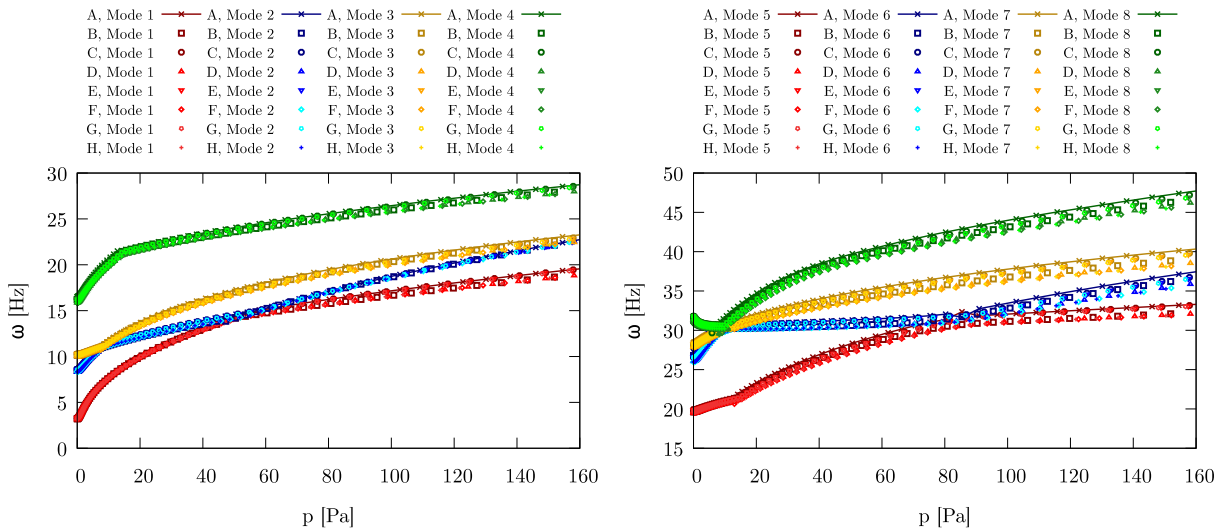

(a) Modes 1-4 **(b)** Modes 5-8

Fig. 20. Variation of the first eight natural frequencies of the biological multilayered plate ($k = 0.226$) along the equilibrium path, large strain regime. Influence of structural theory and reference mid-surface discretization.

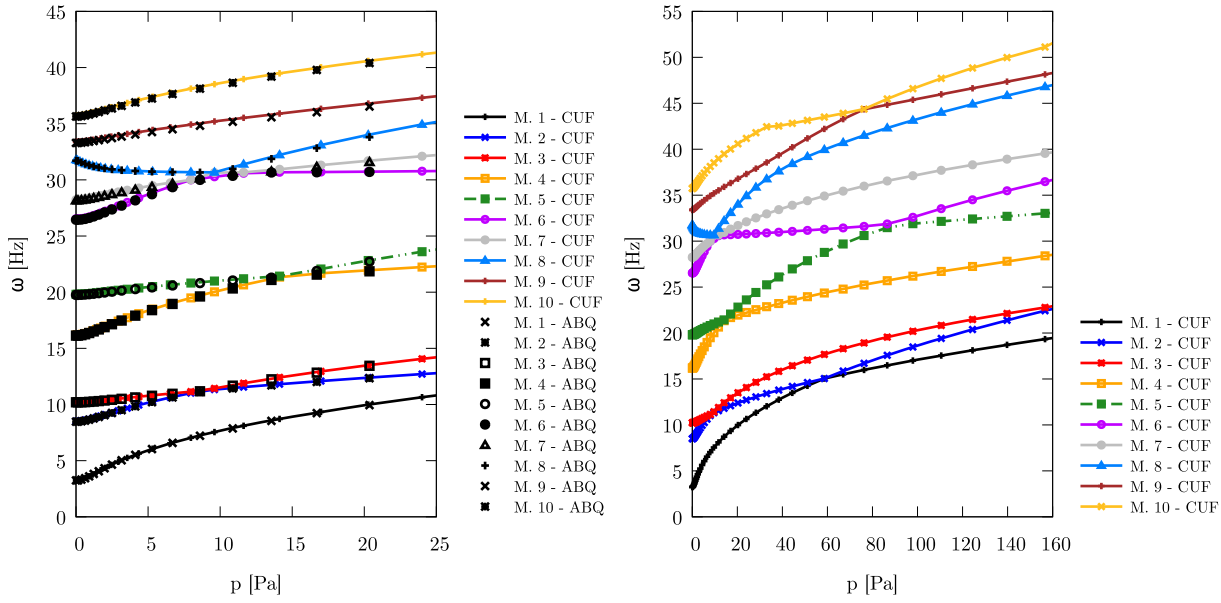

(a) Small strain regime **(b)** Global strain regime

Fig. 21. Variation of the first ten natural frequencies of the biological multilayered plate ($k = 0$) along the equilibrium path. Comparison between high-order 2D CUF models and 3D ABAQUS reference solution.

5.3. Effects of large strain on biological tissue modal behavior

The last case study is the large strain analysis of a nearly incompressible arterial wall specimen subjected to uniform traction pressure. The specimen of the iliac adventitial strips considered in Gasser et al. [11] is now analyzed considering the effects of fiber stiffening, excluding the compressed fibers. In the following, the influence of fiber dispersion and large strain on the static and dynamic responses of the structure is investigated. To compare the proposed model against a reference numerical solution, obtained by adopting hexahedral models, thus comparing against the direct solution of the governing equations without any superimposed kinematic theory, the strain energy function model adopted is the Holzapfel-Gasser-Ogden (HGO) model proposed by ABAQUS commercial software

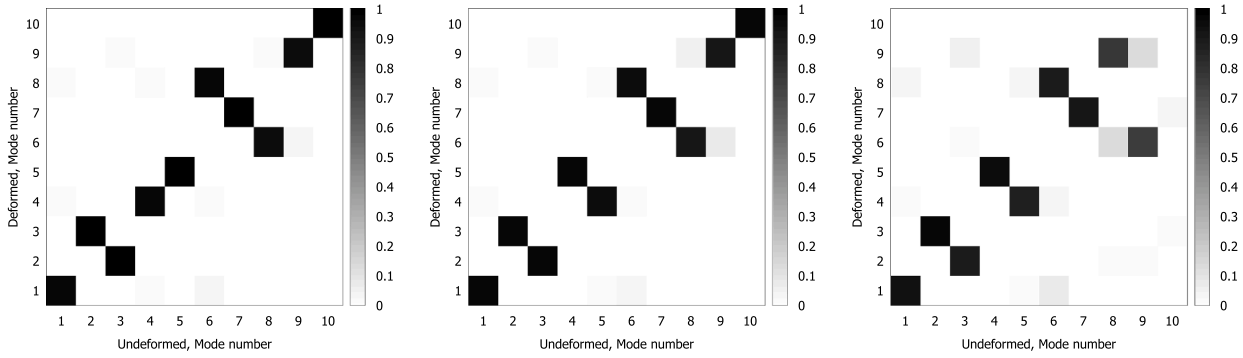

(a) $p = 8.60$ Pa **(b)** $p = 15.38$ Pa **(c)** $p = 53.32$ Pa

Fig. 22. MAC matrix computed comparing the undeformed modal shapes with respect to different deformed configuration modal shapes. Biological multilayered plate, $k = 0$ case. The deformed configuration state is indicated in the sub-caption.

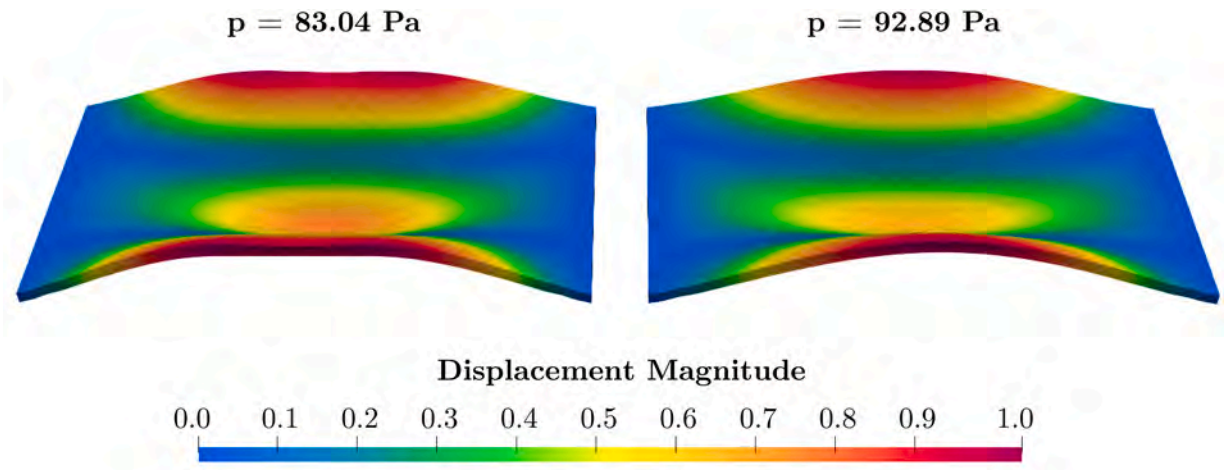

(a) Mode 5, for the two indicated deformed configurations

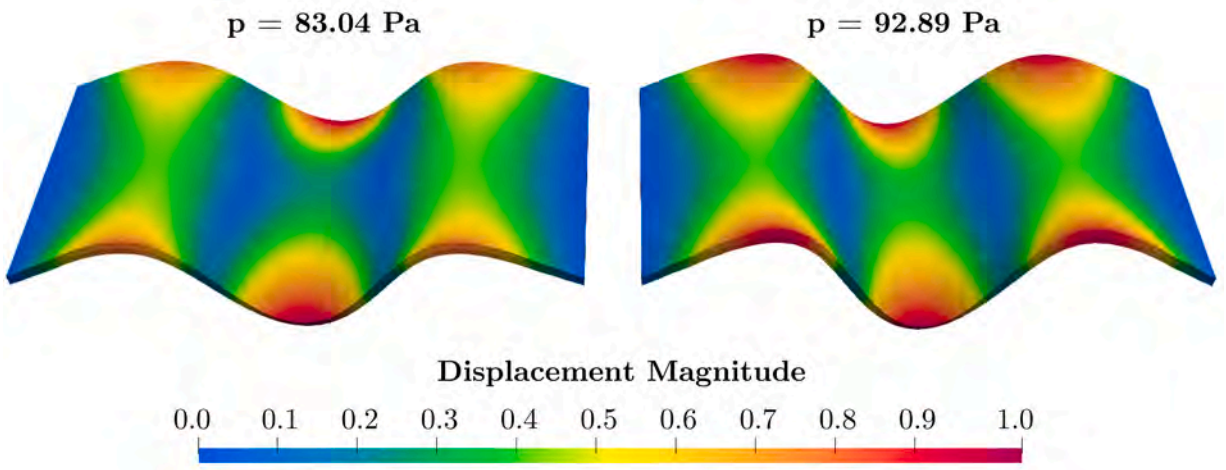

(b) Mode 6, for the two indicated deformed configurations

Fig. 23. Eigenvector representation on the undeformed structures, modes 5 and 6, veering observed. Biological multilayered plate, $k = 0.226$ case.

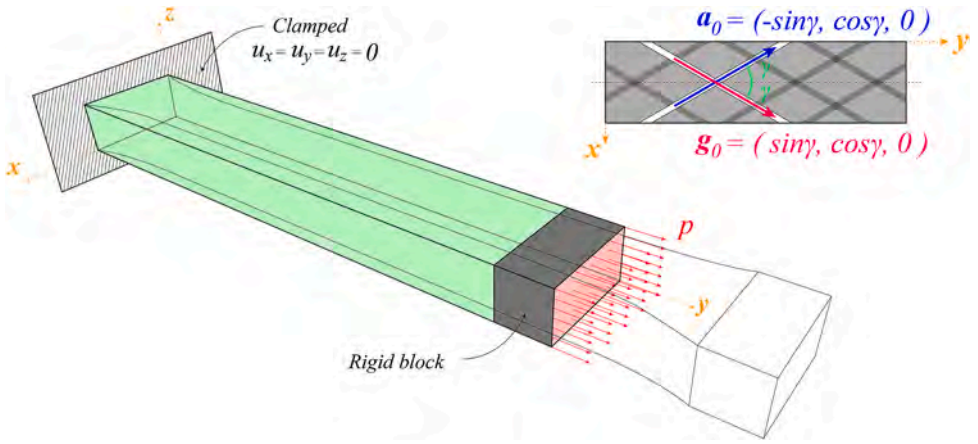

Fig. 24. Large strain analysis of an aortic iliac strip; geometrical and material features considered.

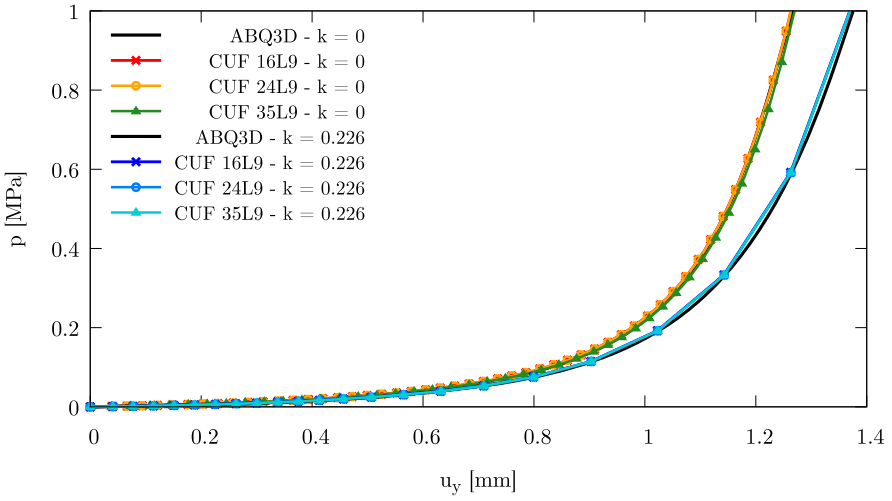

Fig. 25. Large strain analysis of an aortic iliac strip; computed equilibrium path for different LE cross-section expansion models. Comparison between high-order 1D CUF models and different fiber dispersion parameters against the reference 3D ABAQUS solutions.

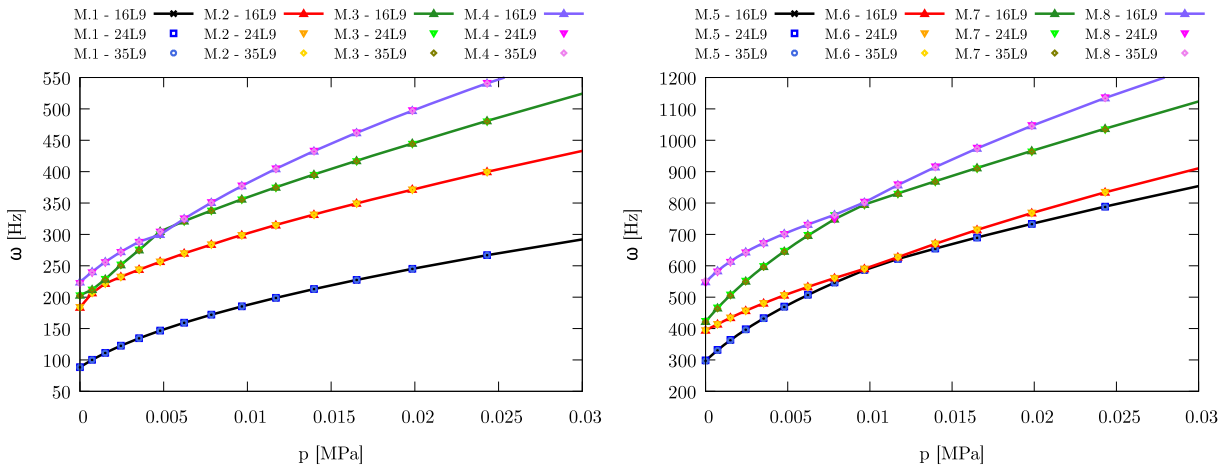

(a) Modes 1-4 **(b)** Modes 5-8

Fig. 26. Large strain analysis of an aortic iliac strip, dispersed fiber $k = 0.226$ case: variation of the natural frequencies in the small strain regime. Comparison between different LE expansion models.

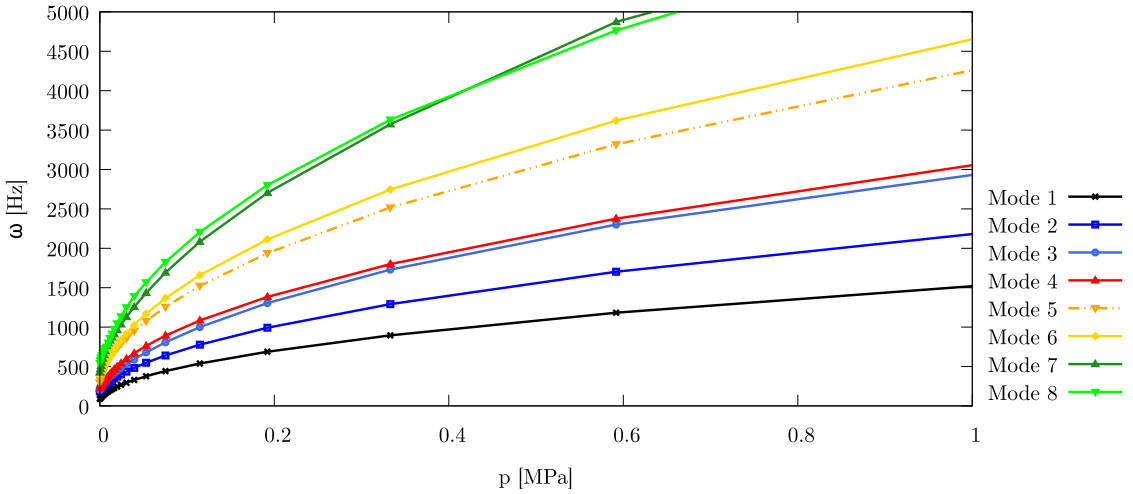

Fig. 27. Large strain analysis of an aortic iliac strip, dispersed fiber $k = 0.226$ case: variation of the natural frequencies in the whole computed equilibrium strain regime. Representation of dispersion curves for the first eight normal modes of vibration.

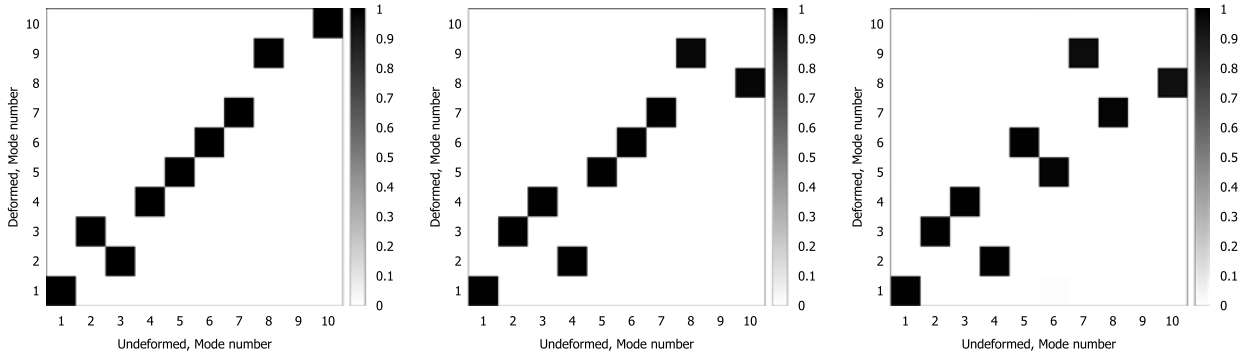

(a) $p = 1.51$ kPa **(b)** $p = 6.22$ kPa **(c)** $p = 13.97$ kPa

Fig. 28. Large strain analysis of an aortic iliac strip, dispersed fiber $k = 0.226$ case: MAC matrices, comparing the normal modes of vibration around the deformed equilibrium states against the reference undeformed normal models of vibration. Deformed configurations reported in the caption.

Eq. (59) [56]:

$$\Psi = \frac{K}{2}\left(\frac{J^2-1}{2} - \log J\right) + \frac{\mu}{2}(\bar{I}_1 - 3) + \sum_{j=4,6} \frac{k_1}{2k_2}\left[e^{k_2 < k\bar{I}_1 + (1-3k)\bar{I}_j - 1>^2} - 1\right] \tag{59}$$

where μ, k_1, k_2, K, and k are the same model parameters described in the previous case study; instead, the symbol $< x >= 1/2(x + |x|)$ denotes the Macauley bracket. A rectangular cross-section beam with dimensions $w = 2$ mm, $h = 1$ mm, and $L = 10$ mm is considered clamped at one end section and subjected to uniform traction pressure at the other free-end section. To simulate an uniaxial tension test, the aortic specimen is tractioned using a rigid block rather than applying the load directly to the free end. The geometrical features and material properties considered are depicted in Fig. 24. The material constants adopted are the same as those reported in the previous case study; thus, again, the aortic specimen is modeled in the nearly incompressible field. The fiber distribution considered is represented by the two symmetric unitary vectors $\boldsymbol{a}_0$ and $\boldsymbol{g}_0$ oriented in the $x - y$ plane inclined at an angle $\gamma = 30°$ with respect to the y-axis, as shown in Fig. 24.

The capabilities of the present approach are discussed by comparing the results obtained via high-order 1D CUF models against numerical reference results obtained with ABAQUS. In this specific case study, the tension-compression behavior is simulated using the built-in ABAQUS model. The proposed 1D CUF model is used to compute and investigate the static equilibrium path and modal response of the aortic iliac strip at large strains, with a reference 3D solution provided for comparison. The ABAQUS models use 6734 C3D20 elements, for a total of 95,514 DOF in the simulation.

First, a convergence analysis on the modal behavior of the aortic strip is conducted to assess the performance of the present approach. Based on previous investigations, a cubic B4 beam-axis FE will be adopted in the following, and different cross-section discretizations with parabolic L9 subdomains will be investigated to prevent volumetric locking [41]. In the following, the aortic

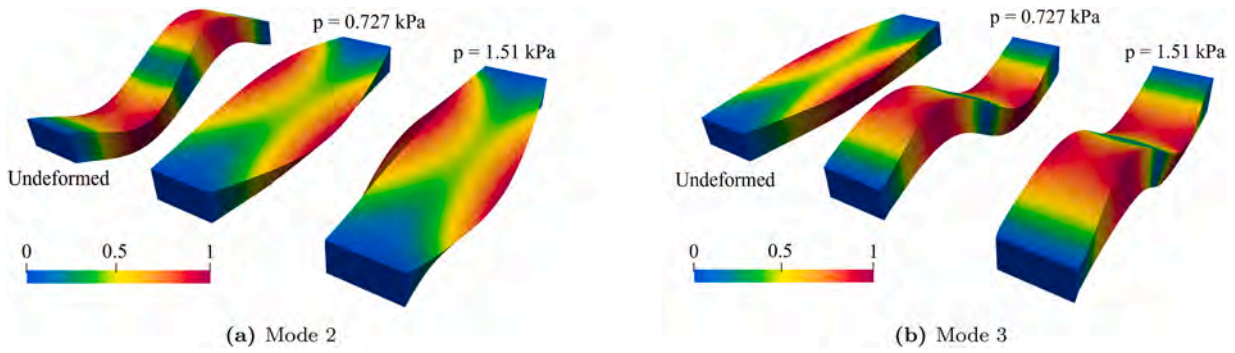

Fig. 29. Large strain analysis of an aortic iliac strip, dispersed fiber $k = 0.226$ case: graphical representation of modes II and III for different deformed configurations. Comparison between different pre-stress applied.

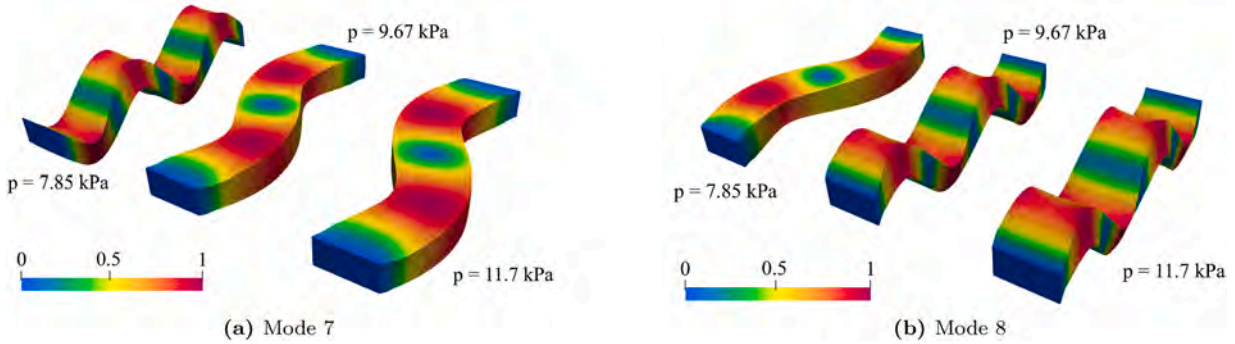

Fig. 30. Large strain analysis of an aortic iliac strip, dispersed fiber $k = 0.226$ case: graphical representation of modes VII and IIX for different deformed configurations. Comparison between different pre-stress applied.

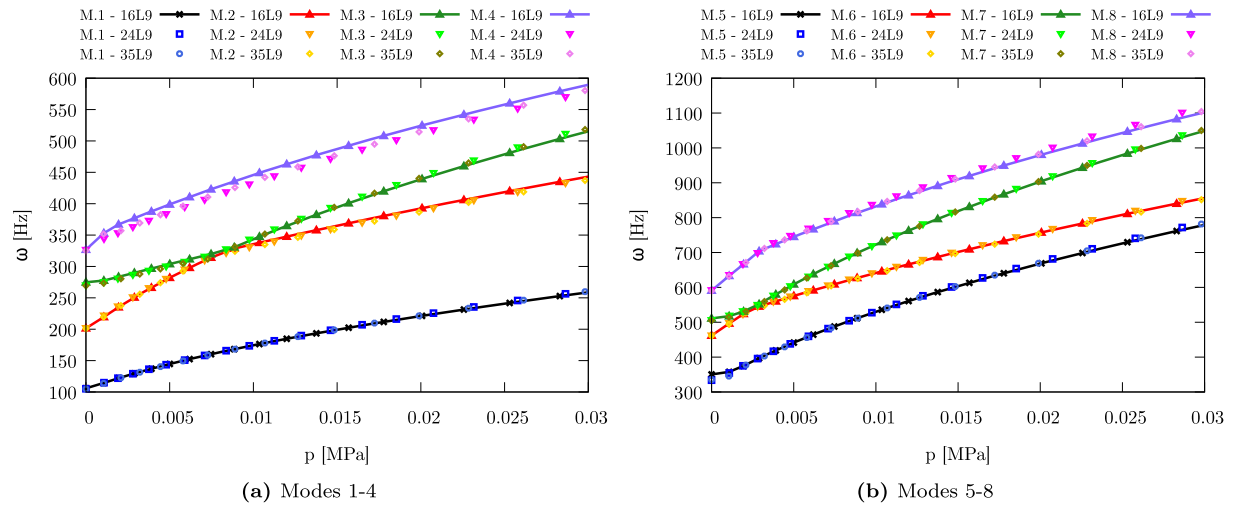

Fig. 31. Large strain analysis of an aortic iliac strip, aligned fiber $k = 0$ case: variation of the natural frequencies in the small strain regime. Comparison between different LE expansion models.

strip will be considered clamped at the two free ends; thus, the clamped condition ($u_x = u_y = u_z = 0$) is applied at the beam cross-section $x = 0$ and $x = L$. Table 3 presents the convergence analysis, comparing the first three natural frequencies of the linearized vibration problem around the trivial undeformed equilibrium state. The modal properties are compared in both cases: dispersed fibers ($k = 0.226$) and perfectly aligned fibers ($k = 0$). The influence of the theory of structure approximation, considering different L9 expansion models, and the effects of kinematic models along the beam axis are extensively analyzed in the proposed case study. The results suggest that each proposed mathematical discretization enables the computation of accurate natural frequencies, with relative

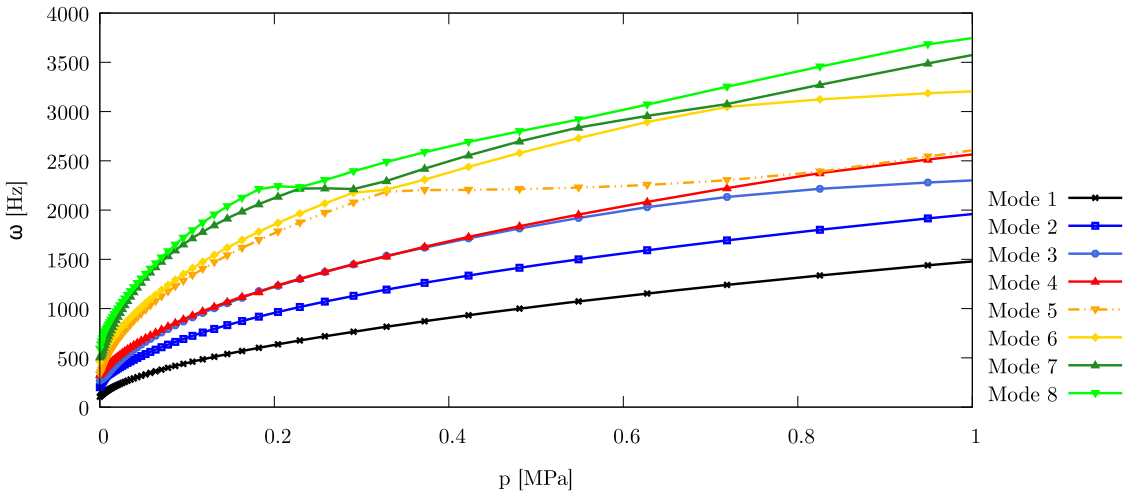

Fig. 32. Large strain analysis of an aortic iliac strip, aligned fiber $k = 0$ case: variation of the natural frequencies in the whole computed equilibrium strain regime. Representation of dispersion curves for the first eight normal modes of vibration.

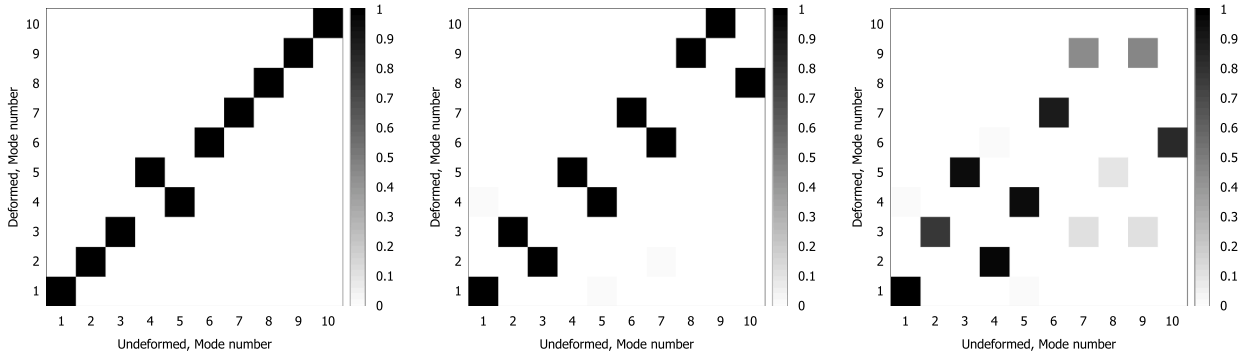

(a) $p = 1.92$ kPa **(b)** $p = 8.37$ kPa **(c)** $p = 95.75$ kPa

Fig. 33. Large strain analysis of an aortic iliac strip, aligned fiber $k = 0$ case: MAC matrices, comparing the normal modes of vibration around the deformed equilibrium states against the reference undeformed normal models of vibration. Deformed configurations reported in the caption.

errors of less than 3% across all analyzed discretizations. In particular, higher relative errors are observed for perfectly aligned fibers, which also exhibit higher natural frequencies. A stiffer response is observed in the case of modal analysis for the $k = 0$ case, thus suggesting that refined discretization models are required in the case of perfectly aligned fibers.

Furthermore, the most accurate results in both material condition cases are obtained when 20 B4 cubic elements are used along the beam axis. For refined cross-section discretization, the relative errors across solutions are less than 1%. Finally, a sensible reduction in DOF can be observed, with a high degree of accuracy achieved by considering models with 69%–88% reductions in DOF, demonstrating the accuracy and consistency of the proposed approach. The adoption of higher-order models helps mitigate numerical instabilities and locking phenomena, enabling the computation of accurate results with coarser discretizations [41]. From this point, further numerical investigation will be conducted using the convergent beam axis model with 20 B4 elements. Instead, the effects of the theory of structure approximation will be further investigated.

Afterwards, considering the most accurate discretization models, the nonlinear large strain analysis of the aortic iliac specimen is performed as the next step. The beam is analyzed under two different conditions, as done in the previous case study: dispersed fibers ($k = 0.226$) and perfectly aligned fibers ($k = 0$).

Fig. 25 depicts the global equilibrium path of the aortic iliac specimen, comparing the results obtained with different 1D CUF models against the 3D ABAQUS solution, for different fiber dispersion configurations. A stiffer response of the beam can be naturally observed in the case of perfectly aligned fibers, as expected by the previously carried out modal free vibration analysis.

The non-trivial equilibrium states marked in the equilibrium paths are the deformed configurations around which the linearized vibration problem is defined. Again, for both fiber dispersion configurations, the variations of modal properties for different stretch configurations are analyzed. Fig. 26 depicts the pressure-frequencies curve in the case of dispersed fiber $k = 0.226$, in the small displacement regime. Specifically, the variation of the first four natural frequencies, obtained by the previously listed cross-section

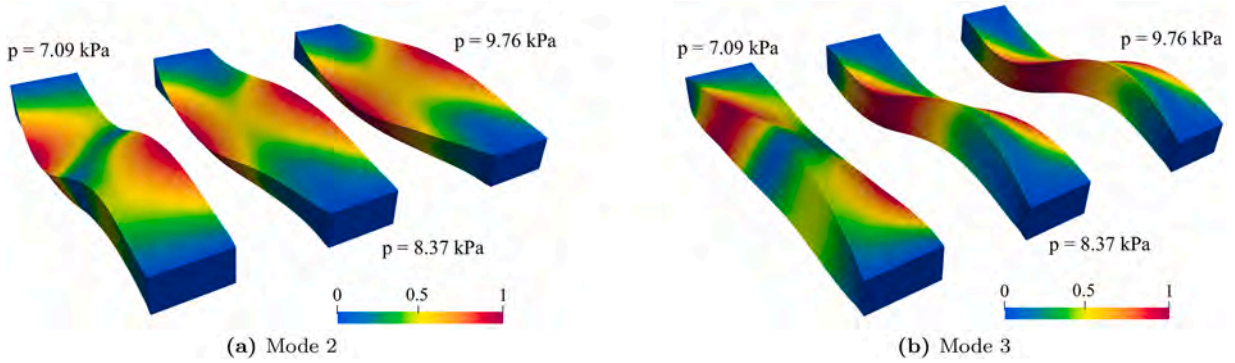

Fig. 34. Large strain analysis of an aortic iliac strip, aligned fiber $k = 0$ case: graphical representation of modes II and III for different deformed configurations. Comparison between different pre-stress applied.

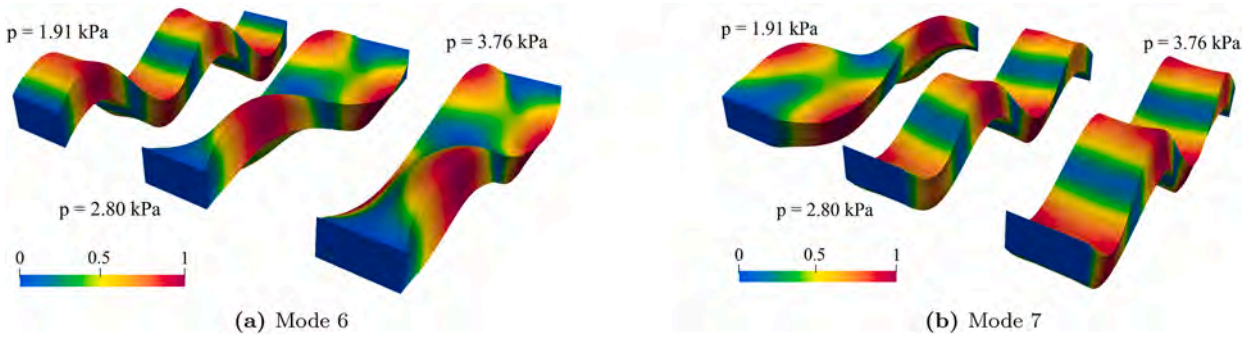

Fig. 35. Large strain analysis of an aortic iliac strip, aligned fiber $k = 0$ case: graphical representation of modes VII and IIX for different deformed configurations. Comparison between different pre-stress applied.

models, is proposed in Fig. 26(a), and (b) proposes the same comparison for the second four natural frequencies (modes five to eight). The same results are depicted in Fig. 27, which shows the same variations measured along the entire computed equilibrium path, highlighting the modal interaction in the large-strain regime for the multilayered biological plate with dispersed fibers. The results show, in the neighborhood of the undeformed trivial equilibrium state, a variation in the first eight natural frequencies and, in particular, modal interaction between modes 2-3-4, 5-6, and 7-8 in structural configurations where the stretch along the beam axis is near unity. In these pre-stressed deformed configurations, for which a negligible axial displacement is observed, the variation of the natural frequencies is justified by a stiffening effect given by the fiber traction energy activation. At the beginning of the uniaxial tension test, the total energy transmitted to the system is converted by the material to reorganize its internal microstructure, resulting in a consequent increase in stiffness due to fiber rotation and alignment processes [11]. Additionally, accurate results are obtained for each cross-section discretization model, and perfectly matching solutions are observed in each non-trivial equilibrium state.

As in the previous case studies, modal interactions are again analyzed using the MAC matrix. Fig. 28 shows different MAC matrices, comparing the normal modes of vibration of the undeformed reference state with the linearized solutions around different deformed configurations. The deformed state is indicated in the caption. The modal interaction observed at small strains, shown in Fig. 26, is here further investigated considering the mode shapes computed in each non-trivial equilibrium state. Fig. 29 compares the second and third mode shapes for different deformed configurations. The same comparison is proposed in Fig. 30 for the seventh and eighth modes of vibration. Differently from the previously discussed cases, the modal interactions observed from the mode shapes are crossing. This can also be confirmed by the correlation between modes found from the MAC matrices.

The same analysis carried out before is now presented for the case of perfectly aligned fibers. Fig. 31 depicts the pressure-frequencies curve in the case of dispersed fiber $k = 0$, in the small displacement regime. Specifically, the variation of the first four natural frequencies, obtained by the previously listed cross-section models, is proposed in Fig. 31(a), at the same time Fig. 31(b) proposes the same comparison for the second four natural frequencies (modes five to eight). The same results are shown in Fig. 32 for the entire computed equilibrium path, demonstrating modal interaction in the large-strain regime for the multilayered biological plate with dispersed fibers. The results show that, in the neighborhood of the undeformed trivial equilibrium state, modal interaction is observed for different partially loaded structural configurations with very small stretch ratios. These interactions are again motivated by the fiber traction energy activation and the internal microstructural reorganization at small strain, leading to stiffening of the strip. The proposed results show again a perfectly matching solution across different cross-section discretization models.

The correlation between normal modes of vibration for different deformed structural configurations is investigated again by means of the MAC matrix, depicted in Fig. 33, where different deformed states are compared against the undeformed trivial equilibrium

state. The modal interaction observed at small strains, shown in Fig. 31, is further investigated here by considering the mode shapes computed for each non-trivial equilibrium state. Fig. 34 compares the second and third mode shapes for different deformed configurations. The same comparison is proposed in Fig. 35 for the sixth and seventh modes of vibration. In both analyzed conditions, crossing between normal modes of vibration is observed.

6. Conclusions

This paper presents the higher-order beam and plate finite element (FE) formulation for pure mechanical analysis of biological tissues. The presented models are formulated within the well-established Carrera Unified Formulation (CUF). The proposed numerical approach has been formulated in the classical hyperelastic framework, including anisotropic effects and fiber reinforcements by the invariant formulation of the constitutive law. The nonlinear governing equations have been exploited through the Principle of Virtual Displacements, rewritten in matrix form by the CUF approximation, thereby defining the Fundamental Nuclei (FN), the elementary blocks of the proposed model. In this way, the FE matrices have been defined as formal expressions independent of the theory of structure approximation and kinematic models adopted in the displacement field definition. Subsequently, a numerical model independent of the mathematical discretization and strain-energy function has been defined. In the proposed work, various anisotropic hyperelastic laws are considered, including asymmetric traction/compression effects of fiber families.
The numerical results are provided in terms of natural frequencies, modal shapes, and displacements distributions for varying prestressed conditions. Validation and convergence analysis have been performed, comparing results with those from 3D analyses conducted with commercial software. The results suggest that:

- The present model can handle the definition of any arbitrary anisotropic hyperelastic potential in the definition of the formal expression of each FE matrix.
- A strong influence of both fiber arrangements and dispersion on the modal behavior is observed, particularly referring to the normal models of vibration. Depending on the fiber dispersion parameter k, different modal interactions, such as crossing or veering, can be observed for the same structural configuration. Similar considerations can be drawn regarding fiber orientation, suggesting then about further investigation into tunable materials, smart and intelligent structures, with variable modal features depending on microstructural arrangements.
- Major influences on the modal interactions at small strain are provided by the stiffening effects observed in the neighborhood of the undeformed condition, justified by an internal reorganization of the microstructure, which affects the pure vibration response with an increase in stiffness and resulting higher natural frequencies.

Future works will deal with an extensive analysis of the locking phenomena of the present model, implementing volumetric locking correction via a hybrid approach, and the inclusion of viscoelasticity and other dissipation mechanisms for a complete dynamic characterization of such materials and structures. Furthermore, the extension of the considerations presented in this work to the wave propagation and bifurcation-instability analysis of soft materials and biological tissues is intended, exploiting the capabilities of the already available framework [57], as well as the inclusion of multi-physics stimuli on both static and dynamical characterization of such materials [58]. Finally, a full Component-Wise (CW) analysis of collagen-reinforced biological tissue is intended to assess the influence of fiber-matrix interactions through independent local refinement.

CRediT authorship contribution statement

Piero Chiaia: Writing – original draft, Software, Investigation, Formal analysis, Data curation; **Alfonso Pagani:** Writing – review & editing, Supervision, Software, Methodology, Funding acquisition; **Erasmo Carrera:** Supervision, Methodology, Funding acquisition, Conceptualization.

Data availability

Data will be made available on request.

Declaration of competing interest

The authors declare that they have no known competing financial interests or personal relationships that could have appeared to influence the work reported in this paper.

Supplementary material

Supplementary material associated with this article can be found in the online version at 10.1016/j.jsv.2026.119737.

References

[1] G.A. Holzapfel, R.W. Ogden, Constitutive modelling of arteries, Proc. R. Soc. A Math. Phys. Eng. Sci. 466 (2118) (2010) 1551–1597. https://doi.org/10.1098/rspa.2010.0058

[2] Z.A. Saib, F. Abed, M.H. Ghayesh, M. Amabili, A review of fluid-structure interaction: blood flow in arteries, Biomed. Eng. Adv. 9 (2025) 100171. https://doi.org/10.1016/j.bea.2025.100171

[3] J.H.C. Wang, Mechanobiology of tendon, J. Biomech. 39 (9) (2006) 1563–1582. https://doi.org/10.1016/j.jbiomech.2005.05.011

[4] S.P. Lake, J.G. Snedeker, V.M. Wang, H. Awad, S.R. C, S. Thomopoulos, Guidelines for ex vivo mechanical testing of tendon, J. Orthop. Res. 41 (10) (2023) 2105–2113. https://doi.org/10.1002/jor.25647

[5] K. Shah, M.U. Rehman, Finite element analysis of custom designed and additive manufactured total surface bearing prosthesis for trans-tibial amputees, Appl. Sci. 15 (3) (2025) 1284. https://doi.org/10.3390/app15031284

[6] J.W. Steer, P.R. Worsley, M. Browne, A. Dickinson, Key considerations for finite element modelling of the residuum-prosthetic socket interface, Prost. Orthot. Int. 45 (2) (2020) 138–146. https://doi.org/10.1177/0309364620967781

[7] G.A. Holzapfel, J.D. Humphrey, R.W. Ogden, Biomechanics of soft biological tissues and organs, mechanobiology, homeostasis and modelling, J. R. Soc. Interface 22 (222) (2025). https://doi.org/10.1098/rsif.2024.0361

[8] D.M. Pierce, T.E. Fastl, B. Rodriguez-Vila, P. Verbrugghe, I. Fourneau, G. Maleux, P. Herijgers, E.J. Gomez, G.A. Holzapfel, A method for incorporating three-dimensional residual stretches/stresses into patient-specific finite element simulations of arteries, J. Mech. Behav. Biomed. Mater. 47 (2015) 147–164. https://doi.org/10.1016/j.jmbbm.2015.03.024

[9] C. Wex, S. Arndt, A. Stoll, C. Bruns, Y. Kupriyanova, Isotropic incompressible hyperelastic models for modelling the mechanical behaviour of biological tissues: a review, Biomed. Eng. / Biomedizinische Technik 60 (6) (2015). https://doi.org/10.1515/bmt-2014-0146

[10] G.A. Holzapfel, T.C. Gasser, R.W. Ogden, A new constitutive framework for arterial wall mechanics and a comparative study of material models, J. Elast. 61 (1/3) (2000) 1–48. https://doi.org/10.1023/a:1010835316564

[11] T.C. Gasser, R.W. Ogden, G.A. Holzapfel, Hyperelastic modelling of arterial layers with distributed collagen fiber orientations, J. R. Soc. Interface 3 (6) (2005) 15–35. https://doi.org/10.1098/rsif.2005.0073

[12] N. Firouzi, K.K. Żur, M. Amabili, T. Rabczuk, On the time-dependent mechanics of membranes via the nonlinear finite element method, Comput. Methods Appl. Mech. Eng. 407 (2023) 115903. https://doi.org/10.1016/j.cma.2023.115903

[13] L. Cardamone, A. Valentín, J.F. Eberth, J.D. Humphrey, Origin of axial prestretch and residual stress in arteries, Biomech. Model. Mechanobiol. 8 (6) (2009) 431–446. https://doi.org/10.1007/s10237-008-0146-x

[14] A. Grillo, S. Federico, G. Wittum, Growth, mass transfer, and remodeling in fiber-reinforced, multi-constituent materials, Int. J. Non Linear Mech. 47 (2) (2012) 388–401. https://doi.org/10.1016/j.ijnonlinmec.2011.09.026

[15] A. Almasi, M. Baghani, A. Moallemi, Thermomechanical analysis of hyperelastic thick-walled cylindrical pressure vessels, analytical solutions and FEM, Int. J. Mech. Sci. 130 (2017) 426–436. https://doi.org/10.1016/j.ijmecsci.2017.06.033

[16] A. Nitti, M. Torre, A. Reali, J. Kiendl, M.D. De Tullio, A multiphysics model for fluid-structure-electrophysiology interaction in rowing propulsion, Appl. Math. Model. 124 (2023) 414–444. https://doi.org/10.1016/j.apm.2023.08.003

[17] Y. Chen, B. Wu, J. Li, S. Rudykh, W. Chen, Low-frequency tunable topological interface states in soft phononic crystal cylinders, Int. J. Mech. Sci. 191 (2021) 106098. https://doi.org/10.1016/j.ijmecsci.2020.106098

[18] Z. Zhao, Y. Chen, X. Hu, R. Bao, B. Wu, W. Chen, Vibrations and waves in soft dielectric elastomer structures, Int. J. Mech. Sci. 239 (2023) 107885. https://doi.org/10.1016/j.ijmecsci.2022.107885

[19] Y. Chen, B. Wu, Y. Su, W. Chen, Effects of strain stiffening and electrostriction on tunable elastic waves in compressible dielectric elastomer laminates, Int. J. Mech. Sci. 176 (2020) 105572. https://doi.org/10.1016/j.ijmecsci.2020.105572

[20] G.A. Holzapfel, R.W. Ogden, Modeling the biomechanical properties of soft biological tissues: constitutive theories, Eur. J. Mech. A. Solids 112 (2025) 105634. https://doi.org/10.1016/j.euromechsol.2025.105634

[21] S. Federico, T.C. Gasser, Nonlinear elasticity of biological tissues with statistical fiber orientation, J. R. Soc. Interface 7 (47) (2010) 955–966. https://doi.org/10.1098/rsif.2009.0502

[22] A.V. Melnik, H. Borja Da Rocha, A. Goriely, On the modeling of fiber dispersion in fiber-reinforced elastic materials, Int. J. Non Linear Mech. 75 (2015) 92–106. https://doi.org/10.1016/j.ijnonlinmec.2014.10.006

[23] K. Li, R.W. Ogden, G.A. Holzapfel, A discrete fiber dispersion method for excluding fibers under compression in the modelling of fibrous tissues, J. R. Soc. Interface 15 (138) (2018) 20170766. https://doi.org/10.1098/rsif.2017.0766

[24] J. Fliege, The distribution of points on the sphere and corresponding cubature formulae, IMA J. Numer. Anal. 19 (2) (1999) 317–334. https://doi.org/10.1093/imanum/19.2.317

[25] A. Pandolfi, M. Vasta, Fiber distributed hyperelastic modeling of biological tissues, Mech. Mater. 44 (2012) 151–162. https://doi.org/10.1016/j.mechmat.2011.06.004

[26] K. Li, R.W. Ogden, G.A. Holzapfel, Computational method for excluding fibers under compression in modeling soft fibrous solids, Eur. J. Mech. A. Solids 57 (2016) 178–193. https://doi.org/10.1016/j.euromechsol.2015.11.003

[27] G.A. Holzapfel, R.W. Ogden, On the tension-compression switch in soft fibrous solids, Eur. J. Mech. A. Solids 49 (2015) 561–569. https://doi.org/10.1016/j.euromechsol.2014.09.005

[28] L. Vergori, M. Destrade, P. McGarry, R.W. Ogden, On anisotropic elasticity and questions concerning its finite element implementation, Comput. Mech. 52 (5) (2013) 1185–1197. https://doi.org/10.1007/s00466-013-0871-6

[29] S. Federico, A. Grillo, S. Imatani, G. Giaquinta, W. Herzog, An energetic approach to the analysis of anisotropic hyperelastic materials, Int. J. Eng. Sci. 46 (2) (2008) 164–181. https://doi.org/10.1016/j.ijengsci.2007.09.005

[30] X. Yu, Y. Fu, H.H. Dai, On propagation of waves in pressurized fiber-reinforced hyperelastic tubes based on a reduced model, J. Sound. Vib. 515 (2021) 116476. https://doi.org/10.1016/j.jsv.2021.116476

[31] M. Bacciocchi, A.M. Tarantino, Finite torsion of transversely isotropic compressible hyperelastic circular cylinders, Int. J. Mech. Sci. 303 (2025) 110582. https://doi.org/10.1016/j.ijmecsci.2025.110582

[32] K. Chaimoon, P. Chindaprasirt, An anisotropic hyperelastic model with an application to soft tissues, Eur. J. Mech. A. Solids 78 (2019) 103845. https://doi.org/10.1016/j.euromechsol.2019.103845

[33] J. Kiendl, M.-C. Hsu, M.C.H. Wu, A. Reali, Isogeometric Kirchhoff-Love shell formulations for general hyperelastic materials, Comput. Methods Appl. Mech. Eng. 291 (2015) 280–303. https://doi.org/10.1016/j.cma.2015.03.010

[34] R. Alberini, M. Terzano, G.A. Holzapfel, A. Spagnoli, A discrete fiber dispersion model with octahedral symmetry quadrature for mechanical analyses of skin corrective surgeries, Comput. Methods Appl. Mech. Eng. 438 (2025) 117809. https://doi.org/10.1016/j.cma.2025.117809

[35] F. Auricchio, M. Conti, A. Ferrara, S. Morganti, A. Reali, Patient-specific finite element analysis of carotid artery stenting: a focus on vessel modeling, Int. J. Numer. Method Biomed. Eng. 29 (6) (2012) 645–664. https://doi.org/10.1002/cnm.2511

[36] A. Mantegazza, D. De Marinis, M.D. de Tullio, Red blood cell transport in bounded shear flow: on the effects of cell viscoelastic properties, Comput. Methods Appl. Mech. Eng. 428 (2024) 117088. https://doi.org/10.1016/j.cma.2024.117088

[37] E. Carrera, Stress resultants governing equations of any beam theory by direct manipulation of 3D equilibrium, Mech. Adv. Mater. Struct. 31 (26) (2023) 7825–7836. https://doi.org/10.1080/15376494.2023.2250543

[38] P. Chiaia, A. Pagani, M. Cinefra, E. Carrera, Analysis of transversely isotropic compressible and nearly-incompressible soft material structures by high order unified finite elements, Mech. Adv. Mater. Struct. 31 (27) (2023) 9451–9467. https://doi.org/10.1080/15376494.2023.2273962

[39] E. Carrera, M. Cinefra, E. Zappino, M. Petrolo, Finite Element Analysis of Structures Through Unified Formulation, Wiley, Chichester, West Sussex, UK, 2014. ISBN: 9781119941217 https://doi.org/10.1002/9781118536643

[40] M. Petrolo, A. Pagani, E. Carrera, G. Candita, P. Iannotti, Mapping beam cross-section features to higher-order generalized variables using machine learning, Thin-Walled Struct. 218 (2026) 114108. https://doi.org/10.1016/j.tws.2025.114108

[41] P. Chiaia, A. Pagani, E. Carrera, Large strain and 3D stress analysis of laminated fiber-reinforced soft material structures with high order beam finite elements, Comput. Struct. 313 (2025) 107735. https://doi.org/10.1016/j.compstruc.2025.107735
[42] A. Pagani, P. Chiaia, E. Carrera, Vibration of solid and thin-walled slender structures made of soft materials by high-order beam finite elements, Int. J. Non Linear Mech. 160 (2024) 104634. https://doi.org/10.1016/j.ijnonlinmec.2023.104634
[43] Y. Chen, L. Jin, Snapping-back buckling of wide hyperelastic columns, Extreme Mech. Lett. 34 (2020) 100600. https://doi.org/10.1016/j.eml.2019.100600
[44] H. Abramovich, D. Govich, A. Grunwald, Buckling prediction of panels using the vibration correlation technique, Prog. Aerosp. Sci. 78 (2015) 62–73. https://doi.org/10.1016/j.paerosci.2015.05.010
[45] R. Azzara, E. Carrera, A. Pagani, Nonlinear and linearized vibration analysis of plates and shells subjected to compressive loading, Int. J. Non Linear Mech. 141 (2022) 103936. https://doi.org/10.1016/j.ijnonlinmec.2022.103936
[46] F. Zhu, R. Augello, R. Azzara, A. Pagani, E. Carrera, W. Chen, Vibration analysis of curved panel subjected to internal pressure and axial compression, AIAA J. 60 (12) (2022) 6842–6853. https://doi.org/10.2514/1.j061999
[47] P.J. Flory, Thermodynamic relations for high elastic materials, Trans. Faraday Soc. 57 (1961) 829. https://doi.org/10.1039/tf9615700829
[48] G.A. Holzapfel, Nonlinear Solid Mechanics, Wiley, 2000.
[49] A. Pagani, E. Carrera, Unified formulation of geometrically nonlinear refined beam theories, Mech. Adv. Mater. Struct. 25 (1) (2016) 15–31. https://doi.org/10.1080/15376494.2016.1232458
[50] B. Wu, A. Pagani, M. Filippi, W.Q. Chen, E. Carrera, Large-deflection and post-buckling analyses of isotropic rectangular plates by carrera unified formulation, Int. J. Non Linear Mech. 116 (2019) 18–31. https://doi.org/10.1016/j.ijnonlinmec.2019.05.004
[51] M.A. Crisfield, An arc-length method including line searches and accelerations, Int. J. Numer. Methods Eng. 19 (9) (1983) 1269–1289. https://doi.org/10.1002/nme.1620190902
[52] A. Pagani, E. Carrera, Unified one-dimensional finite element for the analysis of hyperelastic soft materials and structures, Mech. Adv. Mater. Struct. (2021) 1–14. https://doi.org/10.1080/15376494.2021.2013585
[53] A. Beheshti, R. Ansari, Finite element analysis of compressible transversely isotropic hyperelastic shells, Acta Mech. 234 (7) (2023) 3061–3079. https://doi.org/10.1007/s00707-023-03536-z
[54] H. Fehervary, L. Maes, J. Vastmans, G. Kloosterman, N. Famaey, How to implement user-defined fiber-reinforced hyperelastic materials in finite element software, J. Mech. Behav. Biomed. Mater. 110 (2020) 103737. https://doi.org/10.1016/j.jmbbm.2020.103737
[55] A.W. Leissa, On a curve veering aberration, Zeitschrift für angewandte Mathematik und Physik ZAMP 25 (1) (1974) 99–111. https://doi.org/10.1007/bf01602113
[56] M. Smith, ABAQUS/Standard User's Manual, Version 6.9, Dassault Systèmes Simulia Corp, United States, 2009.
[57] M. Filippi, A. Pagani, E. Carrera, High-order finite beam elements for propagation analyses of arbitrary-shaped one-dimensional waveguides, Mech. Adv. Mater. Struct. 29 (13) (2020) 1883–1891. https://doi.org/10.1080/15376494.2020.1842951
[58] M. Cinefra, S. Valvano, E. Carrera, A layer-wise MITC9 finite element for the free-vibration analysis of plates with piezo-patches, Int. J. Smart Nano Mater. 6 (2) (2015) 85–104. https://doi.org/10.1080/19475411.2015.1037377